Seismic imaging of fault-controlled dolomites in carbonate successions: insights from seismic modeling and RMS amplitude analysis

Wouter Bell Gravendeel
Master in Earth Science

Department of Earth Science
University of Bergen
October 2022

Abstract

This study presents an RMS amplitude analysis of fault-controlled dolomites in a carbonate succession, focussing on the distribution and interpretation of dolomite geobodies. The analysis was conducted to improve the understanding of how seismic survey parameters affect the ability to predict dolomite deposits and whether downscaling the attribute surface would increase the success rate of predictions. The study area was part of the Hammam Faraun Fault block located along the eastern shore of Sinai, Egypt. The Lower Thebes Formation was the formation of interest containing fault-controlled dolomites.

A model of the study area was provided and used to generate synthetic seismic cubes with a wide variety of seismic survey parameters. These cubes were used to generate RMS amplitude surfaces throughout the Lower Thebes formation. A custom script was created to analyze the potential to interpret dolomite geobodies with the surfaces. The script will downscale the RMS amplitude surfaces to different degrees and compare how the scaling and seismic survey parameters affect the predictions' quality.

The findings of this study indicate that for fault-controlled dolomites in a carbonate succession, the significant best predictive quality is obtained when using high frequency, high illumination angle, a low angle of incidence, and, depending on the dolomite concentration, between 1:10 and 1:1 scaling. The highest impact is caused by the illumination angle and angle of incidence, while frequency has the lowest impact. The downscaling works best when the desired dolomite threshold is kept low and performs better than an unscaled RMS amplitude surface up to a dolomite threshold of 30%.

Acknowledgments

First and foremost, I would like to express my sincere gratitude to my supervisors, professor Atle Rotevatn, professor Cathy Hollis and professor Isabelle Lecomte, for their encouragement and guidance. Their expertise, helpful feedback, and patience throughout this project have been invaluable help. An extra thanks to Atle Rotevatn for introducing me to the exciting model without which I could never have written a thesis from which I learned so much.

I would also like to thank Bjarte Hannisdal for getting me into python. Without his courses, I likely would not have considered making the necessary scripts myself. I also want to thank him for his advice regarding the statistical analysis of the seismic data and his insight into methods and tests best suited for the task - furthermore, thanks to Leo Zijerveld for helping me with the SeisRox and Petrel software.

Not to forget, Jonny Hesthammer deserves thanks for his input and encouragement on my choice of topic and suggestions on which supervisors to approach.

Likewise, I am grateful to my fellow students at UiB, especially Vilde Dimmen for her support and encouragement, coworkers at Glex and MVestEnergy, and not to forget my dear friends Jasper, Jialei, Mari, and Lourens, for the support they have given me. Especially to Glex for their patience and consideration with my workload in the weeks approaching my deadline.

Last but not least, I would also like to thank my family for all their support for over the past 2 years.

Table of Contents

1 Introduction

1.1 Project framework

This thesis aims to enhance our comprehension of seismic imaging of carbonate formations and reservoirs contained within them. The thesis investigates seismic response of different carbonate lithologies using seismic RMS amplitude data, particularly dolomite versus non-dolomite lithologies, and analyses the impact on the seismic signature in the subsurface. The thesis work is done in collaboration with Vilde Dimmen's ongoing Ph.D. work: "Imaging fault-controlled hydrothermal dolomite bodies in the subsurface: insights from seismic modeling of the Hammam Faraun Fault system, Suez Rift, Egypt". This thesis is separated from Dimmen's work by its focus on using *RMS amplitude analysis and downscaled versions* to investigate the seismic data of the studied carbonate successions. The synthetic seismic data is generated using a geocellular model based on outcrop data of the Hammam Faraun fault block; Hillary Corlett performed data acquisition and the construction of the model in a collaborative project in 2012 (H. J. Corlett et al., 2018). The Carbonates of interest are the dolomites present in the lower part of the Eocene Thebes Formation deposited prior to the opening of the Gulf of Suez, as dolomites are often the best reservoir rock in carbonate systems (Allan & Wiggins, 1993).

1.2 Motivation

Mapping the geology of the subsurface is important for several reasons. The most important reasons include the detection of hydrocarbons and the detection of potential reservoirs for carbon capture and storage (CCS). This model has been chosen since dolomite has the potential to be an excellent reservoir, but due to its complexity, it is difficult to map. It is impossible to determine the subsurface's geology solely by analyzing the surface. Seismic reflection imaging is the non-invasive, cheapest method for interpreting the geology at the subsurface. The resulting seismic data only indicate relative changes in the acoustic impedance (AI) found at boundaries between lithological layers. Once the data analysis indicates a potential hydrocarbon or CCS prospect, the more expensive invasive method, drilling, can be used to verify the prospect. The seismic data can

be analyzed for flat spots or structures that potentially form a seal/cap rock to determine the optimal drilling location. Coring is the process of extracting cores when drilling and results in an in-situ analysis of the subsurface situation, providing more detailed and extensive data on the reservoir rock. These data are analyzed during drilling and post-drilling using a wireline log. Cores only give a one-dimensional line of data in the 3D subsurface; this, combined with the expensive nature of drilling cores, necessitates that most of the attributes of the subsurface are inter/extrapolated from the core data.

While it is cheaper than drilling, collecting seismic data is no cheap endeavor. Models are used to simulate the subsurface before it gathering seismic data to optimize this collection process. These models are subject to continuous improvement, and this research is part of that optimization.

1.3 Aims and objectives

The first aim of this thesis is to investigate the effect of synthetic seismic data parameters on the ability to use seismic data for dolomite interpretation purposes. These parameters include the elastic properties of the modeled lithologies and the settings used in the modeling software, like frequency, illumination angle, and incidence angle. The second main of this thesis is to evaluate to what extent the RMS amplitude attribute can be used to identify dolomite geobodies in the subsurface. These aims are achieved through the following specific objectives:

- Generate synthetic seismic data from a geocellular model based on outcrop data from the Suez Rift, Egypt.
- Undertake general seismic horizon interpretation
- Undertake seismic RMS analysis of the synthetic seismic
- Analyze the RMS amplitude surfaces using a downscaling.
- Perform a permutation test to determine the significance of using the RMS amplitude to interpret dolomite deposits.
- Determine the effect of the geophysical properties and seismic generation settings on the performance of the prediction/analysis.

1.4 Study area

The thesis focuses on a subsection of the Hammam Faraun fault block (HFFB) located in Egypt on the west coast of the Sinai Peninsula (see figure 1.1). The fault block is part of the Gulf of Suez and was initially modeled as an analog for the rest of the Gulf of Suez (H. Corlett et al., 2021). This thesis uses the model created for "Origin, dimensions, and distribution of remobilized carbonate deposits in a tectonically active zone, Eocene Thebes Formation, Sinai, Egypt" (H. J. Corlett et al., 2018). The dominating fault system is oriented in an NW-SE to NNW-SSE orientation. The dominant dip in the area around the HFFB is tilted 12 to 15° eastward, with the faults having a 60 to 80° dip in a west-northwestern direction.

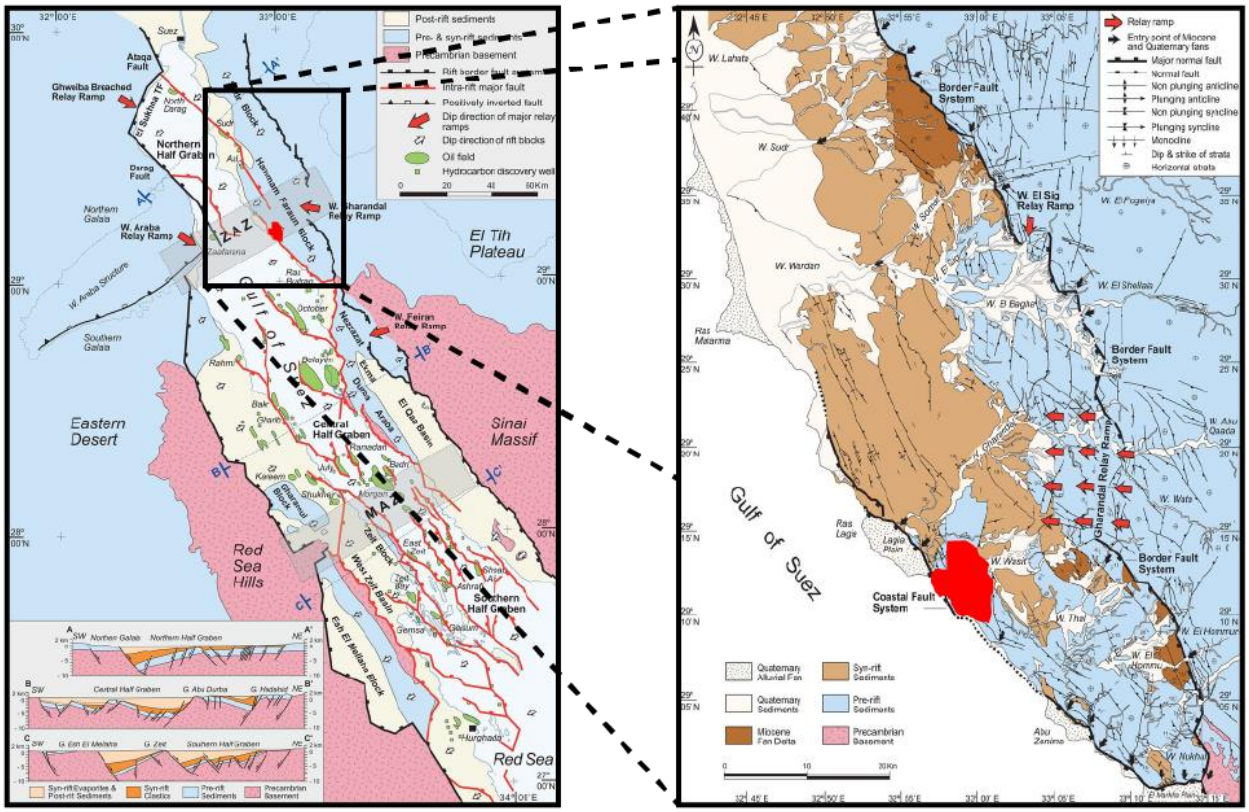

Figure 1.1: An overview of the Gulf of Suez. The Hammam Faraun fault block is located on the eastern bank of the gulf. The modeled area is highlighted in red (Moustafa & Khalil, 2017).

2 Geological history

The Gulf of Suez and the Red Sea were formed when the Arabian and African plates separated. The initial continental rifting started around the late Oligocene to early Miocene (Hamimi et al., 2020). The Dead Sea Transform allowed the two plates to drift further apart and led to the Red Sea being formed (Hamimi et al., 2020). Seafloor spreading started about 5 MA, in the southern part of the Red Sea, during the Neogene (Bosworth, 2015; Ehrhardt & Hübscher, 2015).

2.1 Regional Tectonic framework

2.1.1 Tectonic evolution of the Red Sea

The Red Sea rift system is an extensional rift system that was formed when the Arabian and African continental plates started to separate (Bosworth, 2015). The separation began in the early Oligocene, and the Red Sea basin formed in the Late Oligocene. The rift system is currently divided into two rift stages by the Aqaba-Dead Sea Transform. The Gulf of Suez's Northern part is a failed rift stuck in the continental rift stage. The southern part, the main body of the Red Sea, is an oceanic rift, with the transform allowing the two sections to spread at an independent pace(Moustafa & Khalil, 2017).

2.1.2 The Gulf of Suez

The Gulf of Suez is separated from the Red Sea by the Aqaba-Dead Sea Transform. The Gulf of Suez is a failed rift (Moustafa & Khalil, 2017). The Gulf of Suez can be divided into three sets of half-graben (Moustafa & Khalil, 2017) with an alternating dip, the northern and southern half-grabens dip SW and the central half-grabens dip in a NE direction (see figure 2.1 and 2.2). The HFFB (Hammam Faraun fault block) is located on the east side of the central half-graben (Moustafa & Khalil, 2017).

2.1.3 The Hammam Faraun fault block

The Hammam Faurun fault borders the Hammam Faraun fault block in the east, the Thal fault and Nukhul fault in the west, and the El Markha Transfer / Baba-Markha fault in the south. The fault

block can be divided into smaller segments, such as the Nukhul block (Jackson et al., 2006; Moustafa & Khalil, 2017).

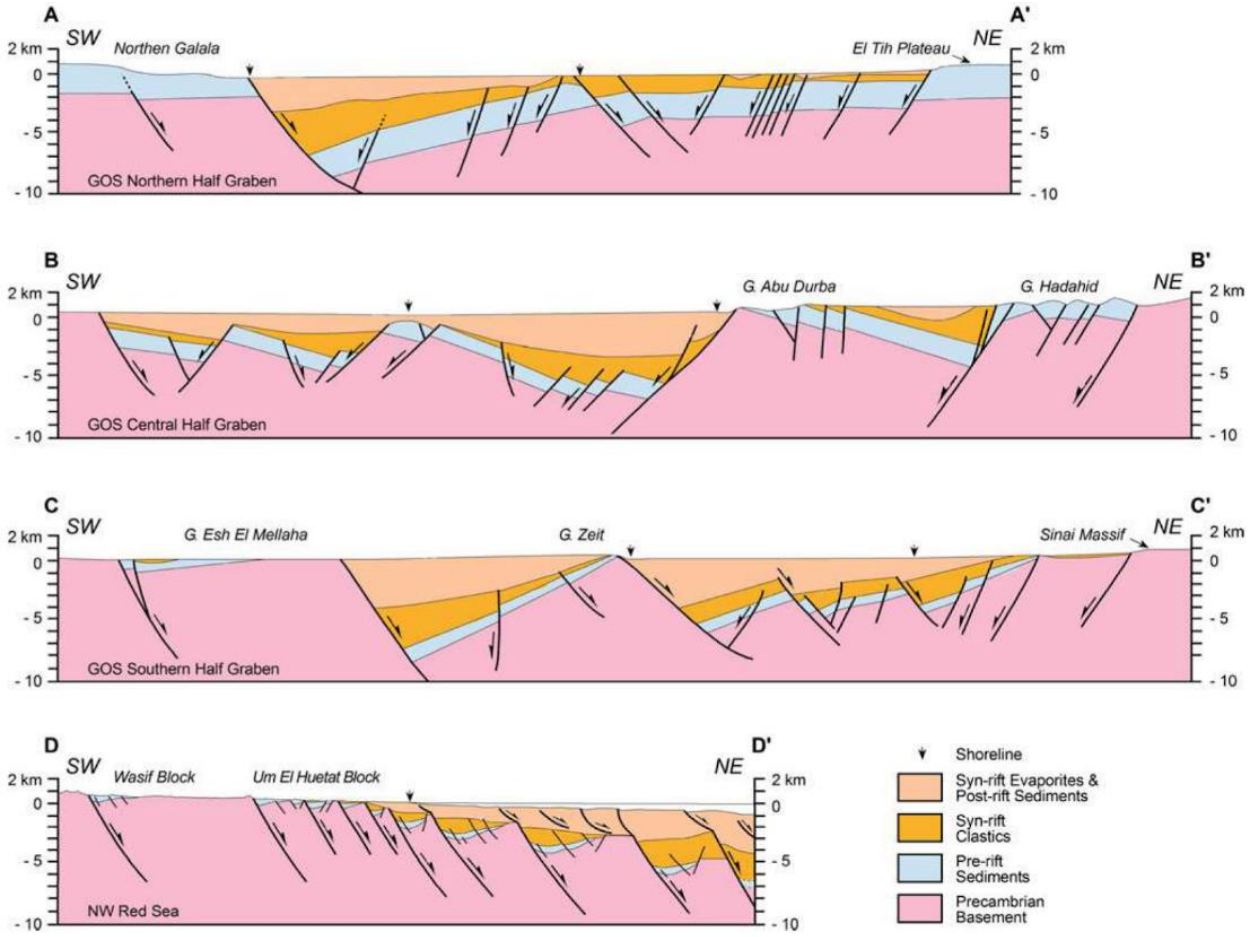

Figure 2.1: Structural cross sections of the half Graben systems in the Gulf of Suez; see figure 1.1 for locations of the cross sections. The target area is not depicted in these cross-sections (Hamimi et al., 2020).

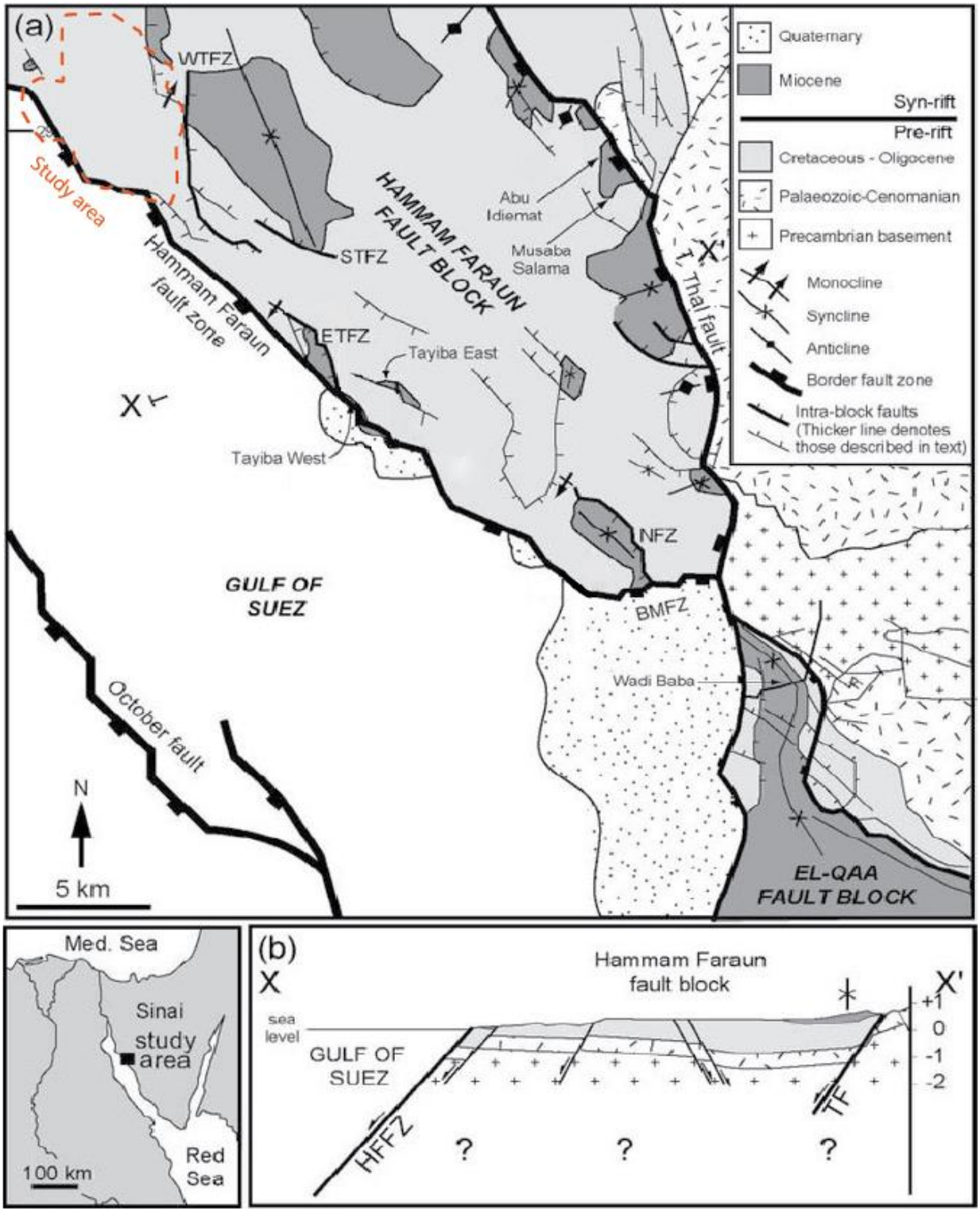

Figure 2.2: a) Map of the Hammam Faraun fault block, study area marked in red b) cross-sections through the Hammam Faraun fault block (Jackson et al., 2006).

2.2 Stratigraphic framework

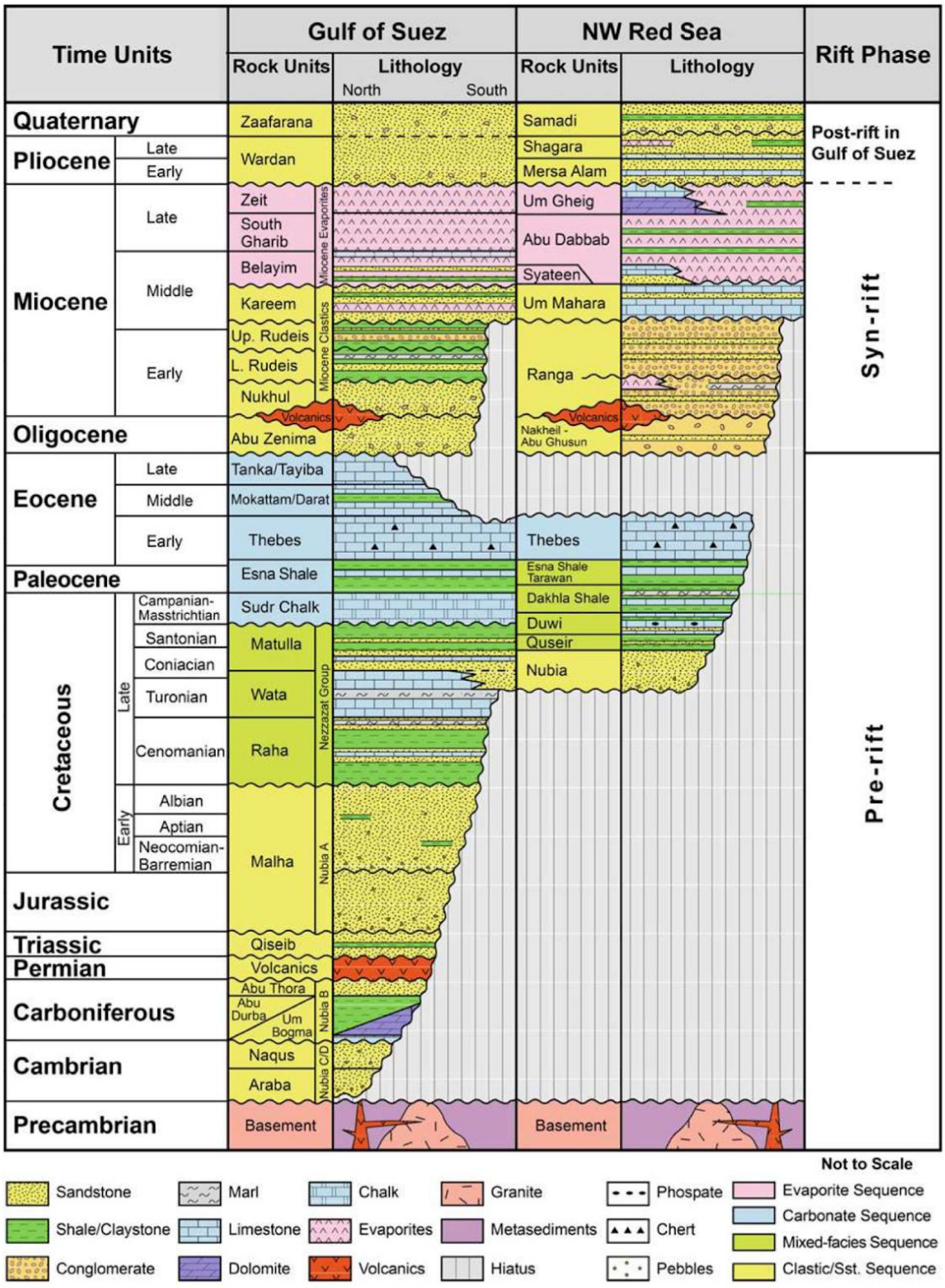

Figure 2.3: Stratigraphic log of the Gulf of Suez (Hamimi et al., 2020).

2.2.1 Pre-rift succession

The HFF block consists of 2000 meters of pre-rift succession overlain by 400 meters of syn-rift succession. The upper part of the pre-rift succession consists of a fining upwards Eocene to Lower Oligocene succession, where a carbonate-dominated Lower Eocene changes into a mudstone-dominated Upper Eocene (Jackson et al., 2006). The carbonates in the Lower Eocene are the area of interest for this thesis. The Pre-rift succession overlies a crystalline Precambrian basement. Depending on the location in the gulf, the age of the lowest clastic deposits will vary. The succession overlaying the basement in the HFF block belongs to the Um Bogma formation (Moustafa & Abdeen, 1992).

Paleozoic to lower Cretaceous

Nubian Sandstones

The pre-rift succession consists of several stratigraphic intervals, the first one a sandstone unit known as the Nubian sandstones. These sandstones contain intervals of shale and carbonates and can be subdivided into several formations (Hamimi et al., 2020; Moustafa & Abdeen, 1992).

Upper Cretaceous

Nezzazat group

Overlaying the Nubian sandstones is a mixed sequence deposited in the late Cretaceous. This composite sequence is also known as the Nezzazat group and can be divided into the Raha, Wata, and Matulla formations. The Nezzazat group is relatively ductile compared to the underlying sandstone and overlying carbonates (Hamimi et al., 2020).

The Raha formation consists mainly of sandstone, limestone shale, and marl and is marine, and there is also a high concentration of fossils in this formation. The Wata formation is a limestone and dolomite-dominated formation with a high fossil content. The lower part of the Matulla formation consists of sandstone, while the upper part is predominantly shale (Moustafa & Abdeen, 1992).

Paleocene and Eocene

Esna shales

The Cretaceous succession is overlain by the Esna shales, spanning the entire Paleocene and some of the Lower Eocene (Moustafa & Abdeen, 1992).

Thebes Formation

Overlaying the Esna formation is the Thebes Formation, the interval of interest for this thesis. The Thebes Formation can be subdivided into three parts. The lower part consists of limestone and contains chert bands, the middle part is a hard, chalky limestone, whereas the upper part is a chalky limestone containing chert bands. The very top of the upper Thebes Formation is marly (Moustafa & Abdeen, 1992).

Darat and Tanka formations

The middle Eocene contains the Darat formation and the Tanka formation. The Darat formation consists mainly of marls and shales and is interbedded by limestone (Moustafa & Abdeen, 1992). The Tanka formation is either middle Eocene (Moustafa & Abdeen, 1992) or upper Eocene depending on the source. The Tanka formation is a limestone layer deposited in a shallow marine environment (Jackson et al., 2006).

2.2.2 Early rift succession

Abu Zenima formation

Lying unconformably on top of the Tanka formation is the Abu Zenima formation (Moustafa & Abdeen, 1992). Until 1999 it was not reliably dated but has been confirmed to be of Oligocene age based on well-preserved microfossils (Hamimi et al., 2020; Refaat & Imam, 1999). This, combined with the fact that it was deposited prior to the early rift volcanic deposits, means it is also an early rift deposit. The formation consists of red and purple mud- silt- and sandstones with some conglomerate beds. In the study area, the thickness of the layer varies, increasing towards the south and completely disappearing in the north (Moustafa & Abdeen, 1992).

Nakheil formation

The Nakheil formation is a formation with red sandstone, limestone, conglomerate, and breccia, the later two consisting of chert and limestone (Hamimi et al., 2020).

Early rift Volcanics

The volcanics are dated between the Abu Zenima formation and the Nukhul formation (post-rift) due to the baked top of the Abu Zenima formation and basalt boulders found within the Nukhul formation (Moustafa & Abdeen, 1992). The volcanic deposits are present in the form of ballistic flows, dikes, and sills.

2.2.3 Syn-rift and Post-rift succession

In the study area, the syn-rift succession consists of the lower Miocene Nukhul and Rudeis formations, which lie unconformably on top of the Oligocene basalts (Moustafa & Khalil, 2017).

Nukhul formation

The Nukhul formation has a conglomerate base bed with the basalt mentioned above and limestone boulders from the Thebes Formation. The lower parts of the Nukhul formation consist of fluvial and estuarine sandstones, while the upper parts are predominantly carbonates and anhydrides deposited in several sub-basins formed due to rifting (Hamimi et al., 2020).

Rudeis formation

The Rudeis formation mainly consists of claystones with limestone with sandstone beds throughout (Moustafa & Abdeen, 1992).

3 Theoretical Background

This chapter will introduce concepts important to the thesis. First, a little about seismic data and its collection in the field, then how it can be simulated through modeling to produce an environment to cost-efficiently test seismic responses and effects of external or internal factors.

3.1 Seismic response

Seismic data is the time, and amplitude record of waves projected into the earth and returned to the surface through reflection or refraction. Seismic data is gathered using a source and one or multiple receivers. The signal is usually seismic, also known as an acoustic energy wave. The source sends a pulse of energy into the subsurface, which is partially reflected off of lithological boundaries in the subsurface. The receiver(s) recorded these reflections and timestamped them relative to the source. By varying the source and receiver location, the subsurface can be mapped.

3.2 Seismic resolution

Seismic resolution is the scale at which two distinct features can be separately identified. The seismic resolution differs between the vertical and horizontal axis due to how wave propagation works. Vertical resolution (r_V) is solely based on the wavelength (λ) of the signal (see formula 3.1) and determines the thickness if beds that can be distinguished (Kallweit & Wood, 1982). The lateral resolution (r_H) of an unmigrated seismic signal is determined by the Fresnel zone (see formula 3.2), which can be calculated using the wavelength and depth (z) of the reflector (Kallweit & Wood, 1982). When migrating the data, the Fresnel zone shrinks into a circle with a diameter of about half the signal's wavelength, increasing the lateral resolution (see formula 3.2) (Simm & Bacon, 2014). The lateral resolution determines how well features can be distinguished laterally.

$$r_V = \frac{\lambda}{4}$$

Formula 3.1: Vertical resolution as a function of wavelength (Kallweit & Wood, 1982).

$$r_H \approx F_d = \sqrt{\left(z + \frac{\lambda}{4}\right)^2 - z^2} \xrightarrow{Migration} r_H \approx \frac{\lambda}{2}$$

Formula 3.2: Lateral resolution before and after migration as a function of wavelength (λ) and depth (z) (Kallweit & Wood, 1982).

3.3 Acoustic impedance

Acoustic impedance is an elastic property of the lithology that can be expressed by formula 3.3, where V is the velocity and ρ is the bulk density of the lithology (Wood & Cai, 2022). A rapid change in acoustic impedance results in a seismic response as it acts as a seismic reflector.

$$Z = \rho \cdot V$$

Formula 3.3: Acoustic impedance as a function of bulk density and velocity.

3.4 Seismic Modeling

Seismic modeling uses a model to act as a proxy for the earth and then simulates the process of gathering seismic explained in section 3.1. Seismic modeling can increase our understanding of the subsurface and how elastic waves behave. Seismic modeling will generate a synthetic seismic based on a subsurface model. The more accurate the model is, the closer the synthetic seismic will come to the real seismic. Seismic modeling is a process that can help link outcrops, and field observations to seismic data retrieved from seismic surveys gathered at sea. Applying seismic modeling to an outcrop model makes it possible to improve our understanding of how structures and boundaries are visualized on a seismic survey and how the scale of the structures in the field affects the seismic response. There are several methods of performing seismic modeling, each with its strengths and weaknesses.

3.4.1 1D convolution modeling

1D convolution modeling uses a single dimension to model the seismic signal, calculating the impedance along the vertical axis and converting this into reflectivity using formulas 3.3 and 3.4. This reflectivity is then combined with the wavelet and noise using addition to produce a seismic

trace. 1D convolution models are highly efficient and widely used in the industry (Lecomte et al., 2015). The efficiency of the 1D convolution modeling comes at a cost; the method lacks complexity. 1D modeling cannot simulate propagation effects or illumination effects as it is strictly limited to one dimension (Lecomte et al., 2015). There are some factors to take into account when using the 1D convolution method, namely 1) generating the appropriate time function to simulate elastic-wave responses, 2) selecting the wavelet that should be used, and 3) the use case of the generated seismic trace (Lecomte, 2015).

$$R = \frac{Z_1 - Z_2}{Z_1 + Z_2}$$

Formula 3.4: Reflectivity as a function of acoustic impedance of the medium above the reflector (1) and the medium below (2)

3.4.2 2D/3D full-wavefield modeling

Full-wavefield (FW) methods use the wave equation to generate the synthetic seismic. The method generates all possible waves using the velocity model, wavelet information, and a survey (Lecomte et al., 2015). However, this process requires a lot of computing power, which is one of the drawbacks of this method. This modeling method is not ideal for analyzing wave propagation, but it does allow for it through the generation of animations (Lecomte et al., 2016). Finite difference (FD) is the best-known version of full wavefield modeling. Finite difference wavefield modeling utilizes a finite-difference operator to approximate the results of the derivatives of the wave equation. FD uses a grid to calculate these approximations, but with a static grid, these calculations become increasingly inaccurate, requiring additional computations to create a variable grid (Lecomte et al., 2016).

3.4.3 2D/3D ray-based modeling

RB (Ray-based) modeling uses the eikonal equation to calculate rays and travel-times in the model, while the transport equation provides the amplitudes for said ray-paths (Lecomte et al., 2015).

PSF

Point-spread functions (PSF) can be created based on either a full-wavefield or ray-based method (Lecomte et al., 2016). A ray-based PSF incorporates realistic angle-dependent illumination and calculates the resolution based on selected parameters (background velocity, wavelet, and survey).

This project utilizes an analytically derived point-spread function to generate the synthetic seismic. The parameters chosen will be listed and explained in detail in chapter 4. The ray-based PSF cannot be used as no survey or background/overburden model is included in the data (Lecomte et al., 2016).

3.5 Seismic interpretation

Seismic interpretation is the analysis of the subsurface based on a seismic line or cube, usually in combination with drilled wells. The seismic interpretation focusses on determining the geological surfaces, faults, and potential hydrocarbon indicators. When interpreting horizons, noteworthy properties are the reflector's continuity, polarity, and potential change in polarity of the reflector. When interpreting seismic data, one of the tasks is to differentiate noise from the signal (Morton-Thompson, D., 1993).

3.6 Wavelet

A wavelet describes the isolated shape seismic pulse that is recorded when a wave reflects off a reflector. When creating a convolution model, a wavelet must be selected to generate the seismic traces by adding a wavelet wherever a reflector would cause a signal. For precise work, the shape of the wavelet should be custom to the situation, but an idealized wavelet can be used in cases where the wavelet is not known. The Ricker wavelet is one such idealized wavelet and is the one chosen for this thesis (Simm & Bacon, 2014).

4 Material and Methods

4.1 The Model

The model was created for a paper by Hillary J. Corlett, and this section will give a brief overview of the work done and choices made during the creation of the model.

The paper "Origin, dimensions, and distribution of remobilized carbonate deposits in a tectonically active zone, Eocene Thebes Formation, Sinai, Egypt" (H. J. Corlett et al., 2018) analyzed part of the HFF block in order to create a subsurface analog (see figure 1.1 in section 1.4). The analysis was done through Lidar, outcrop observations, rock samples, and core plugs.

The study area is an exposed section of the Thebes Formation found east of an anticline at the Galala Plateaus in the HHFB (Höntzsch et al., 2011; Scheibner et al., 2001, 2003). This part of the Thebes Formation was deposited in a carbonate-dominated basin, shallow in the north and deeper towards the south. The basis of the basin was a sizeable NE-SW trending anticline ridge that is part of the Syrian Arc System or Fold Belt (SAFB). The SAFB was formed during the compressional phase of the closure of the Neo-Tethys Ocean. The anticline ridges formed due to extensional faults reactivating during the compressional tectonic phase acted as the platforms necessary for carbonate deposition (Bosworth et al., 1999; El-Motaal & Kusky, 2003; Moustafa, 2014; Moustafa & Khalil, 1995; Youssef, 2003). The resulting deposits in the HHFB are dominated by distal slope to basinal deposits. The Thebes Formation was exposed in fault blocks during late Oligocene rifting (Moustafa & Abdeen, 1992; Young et al., 2003), providing pseudo-3D exposure. This exposure allowed for excellent observations of the dimensions and distribution of the essential remobilized carbonate facies (H. J. Corlett et al., 2018).

The geocellular model used here was created for "Origin, dimensions, and distribution of remobilized carbonate deposits in a tectonically active zone, Eocene Thebes Formation, Sinai, Egypt" (H. J. Corlett et al., 2018). The data for the model was collected from outcrops with exposed parts of the Thebes Formation using stratigraphic logging and mapping techniques as well as direct measurements wherever possible. Inaccessible outcrops were logged using a laser range finder. A

total of 34 stratigraphic sections were logged, adding up to a total of 909.69 meters, 24 of which were logged directly, while ten were logged using Lidar (H. J. Corlett et al., 2018).

Multiple techniques were used to determine the dimension and number of occurrences of remobilized carbonate facies. For this purpose, field and satellite photos were analyzed using ImageJ in combination with the jPOR macro. The dip of the photos was measured and used to calibrate the dimensions of the geobodies. Some facies were measured in the field, directly where possible, otherwise with a laser (H. J. Corlett et al., 2018).

A geocellular reservoir model of the Hammam Faraun fault block was created in Petrel with cells of 25 by 25 by 3 meters. The model is constrained to the Thebes Formation between the Thal fault and the HFF (Hollis et al., 2013).

The background facies consist of slope and distal deposits. The remobilized grain flow, debris flow and slumped geobodies are added to the model using object-based modeling. The size and shape of these geobodies are modeled after the dimensions derived from the field observations (Hollis et al., 2013).

The massive and strata-bound dolomites are added using algorithms. The massive dolomites are modeled using an algorithm based on the distance from the fault. The strata-bound dolomites are modeled using an algorithm based on distance from the fault, facies type, and a probability function (Hollis et al., 2013).

The Thal fault and the Hammam Faraun fault border the Hammam Faraun fault block. The two faults are part of the Suez rift and dip westward at an angle of about 60° to 80°. The Thal fault has an NNW - SSE orientation, and the Hammam Faraun fault has an NW - SE orientation. The lesser faults in the area mostly follow these two orientations (see figure 2.2). The Suez rift is oriented in an NNW - SSE direction and is an extension of the Red Sea rift (Gawthorpe et al. 2003, 885).

The geometry of the HFF block is a half-graben, tilted in an eastern direction by 12° to 15°. The fault block has a maximum width of about 25km (Gawthorpe et al. 2003, 885) and the two main faults defining the fault block are longer than 25km.

The HFF block has internal faulting as well. These faults largely conform to the orientation of the perimeter faults. These internal faults are mainly syn- and antithetic faults on the mesoscale with a displacement of around 1 km. (Gawthorpe et al. 2003, 885)

4.2 Modelling

This thesis utilizes Point-Spread function (PSF) based 3D modeling of an inverse to generate synthetic seismic data for the HFFB. Chapter 3 includes an overview of the theory for this kind of modeling. The model of the HFFB, as described in section 4.1 above, has been used to generate the synthetic seismic; a step-by-step process attached in appendix 1.

The process of generating the synthetic seismic can be customized by changing the parameter values, such as the wavelet, the frequency of said wavelet, the average velocity of the wave, the target area, the illumination angle, and the angle of incidence. Apart from the wavelet, these variables represent the settings and choices made when gathering seismic in real-life seismic data acquisition. By varying these settings in the model, it is possible to analyze their effect on the detection rate of the method and determine the best method for dolomite detection. The variables analyzed in this thesis include frequency, illumination angle, and angle of incidence, which will be described in detail below.

Attenuation (α) can be calculated using the rock quality factor (Q), the wave velocity (v) and the wave frequency (f) (see formula 4.1). The attenuation is proportional to the inverse of the rock quality and directly proportional to the wave frequency (f). Therefor as the wave propagates, the amplitudes of higher frequencies attenuate faster, and the dominant frequency shifts towards a lower frequency (see figure 4.1) (Raji & Rietbrock, 2013).

$$\alpha = \frac{1}{Q} \cdot \frac{\pi \cdot f}{v}$$

Formula 4.1: Seismic attenuation

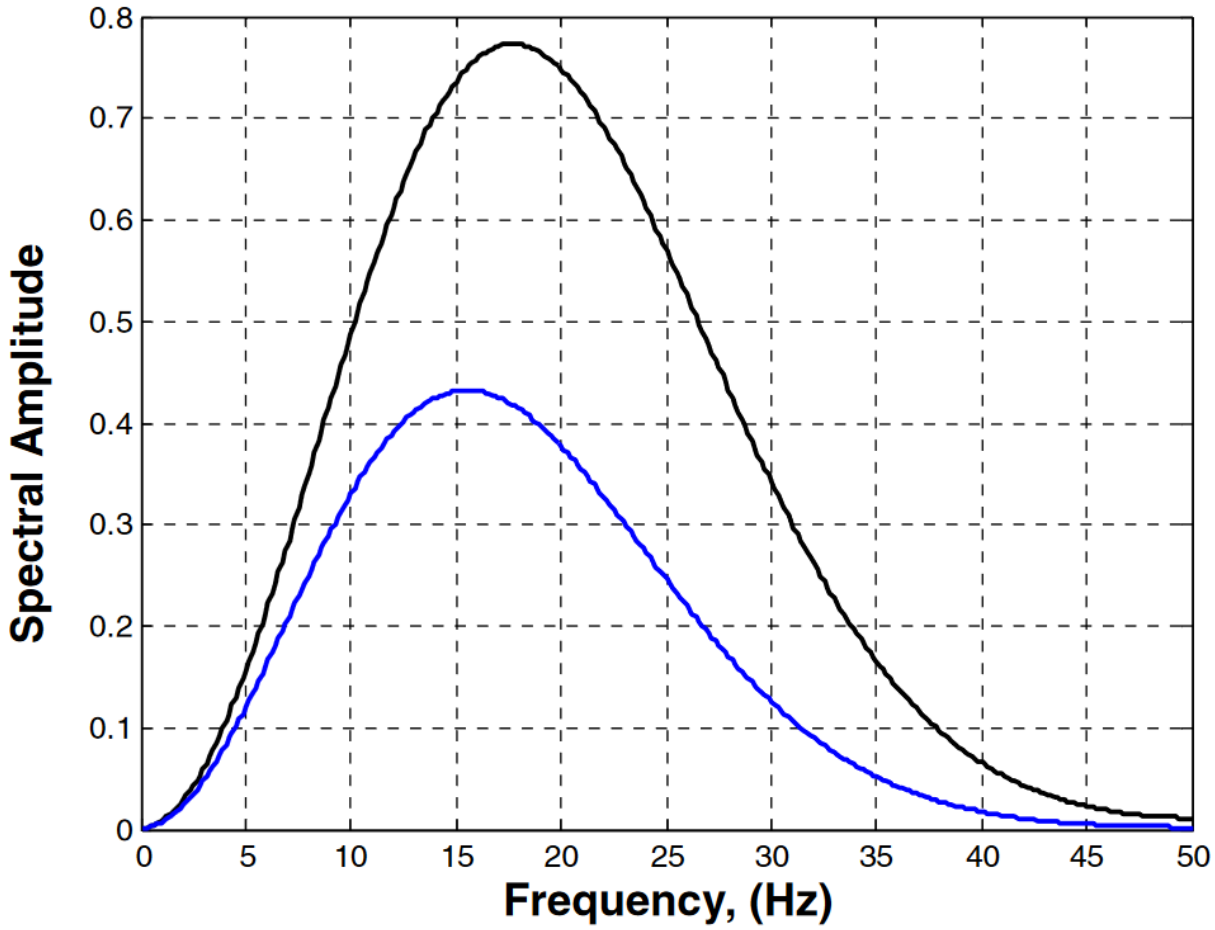

Figure 4.1: Frequency spectrum at t=0 (black) and t=2.2s (blue). The attenuating medium has a Q value of 30. The figure shows the effect attenuation has on the frequency; the highest amplitude decreases, the high frequencies are reduced faster, causing the peak to shift left (Raji & Rietbrock, 2013).

When gathering seismic in real-world situations, these variables are restricted by what the subsurface allows to pass through. The sources used will be as powerful as possible, but the dominant frequency and the frequency band will depend on what the earth allows to propagate.

Illumination angles and angles of incidence will also depend on the subsurface composition and the spacing of sources and receivers; this is because the combination of spacing and refraction between the layers determines the angles that are relevant for the elastic waves.

Since these parameters depend on the subsurface, the thesis does not analyze what parameter values should be applied to an area. This thesis instead focusses on the effectiveness of the determined combination of parameter settings, i.e., how accurately this specific subsurface can be predicted.

SeisRoX has been used to perform the 3D PSF-based convolution modeling. The program requires elastic properties, including the P-wave velocity (V_P), the S-wave velocity (V_S), and density or rock physics models based on petrophysical parameters (such as porosity and mineral composition). In this case, elastic properties were used. The software will generate a reflectivity model, which will then be used together with the selected wavelet to synthesize the 3D PDSM seismic data. Synthesizing the seismic data does not utilize ray tracing but instead uses the input variables to estimate the seismic responses throughout the model (Davies, 2018).

4.3 Model variables

Several cases have been made to analyze the variables' effect on the ability to predict dolomite occurrences. Each case represents a 3D seismic cube generated with the variables set to specific values. The cases have been set up so that each variable is varied one at a time while the others remain controlled. This is the case for all variables except for the illumination angle and the angle of incidence. These two angles have been varied as a pair to simulate the effect the illumination angle has on the angle of incidence (see figure 4.2). As the angle of incidence increases, the illumination angle decreases. There is no direct relationship between the two angles; however, a larger angle of incidence comes with large offsets between the source and receiver. As Snell's law explains, a large offset often also results in a restricted illumination pattern than a smaller offset (Lecomte, 2008).

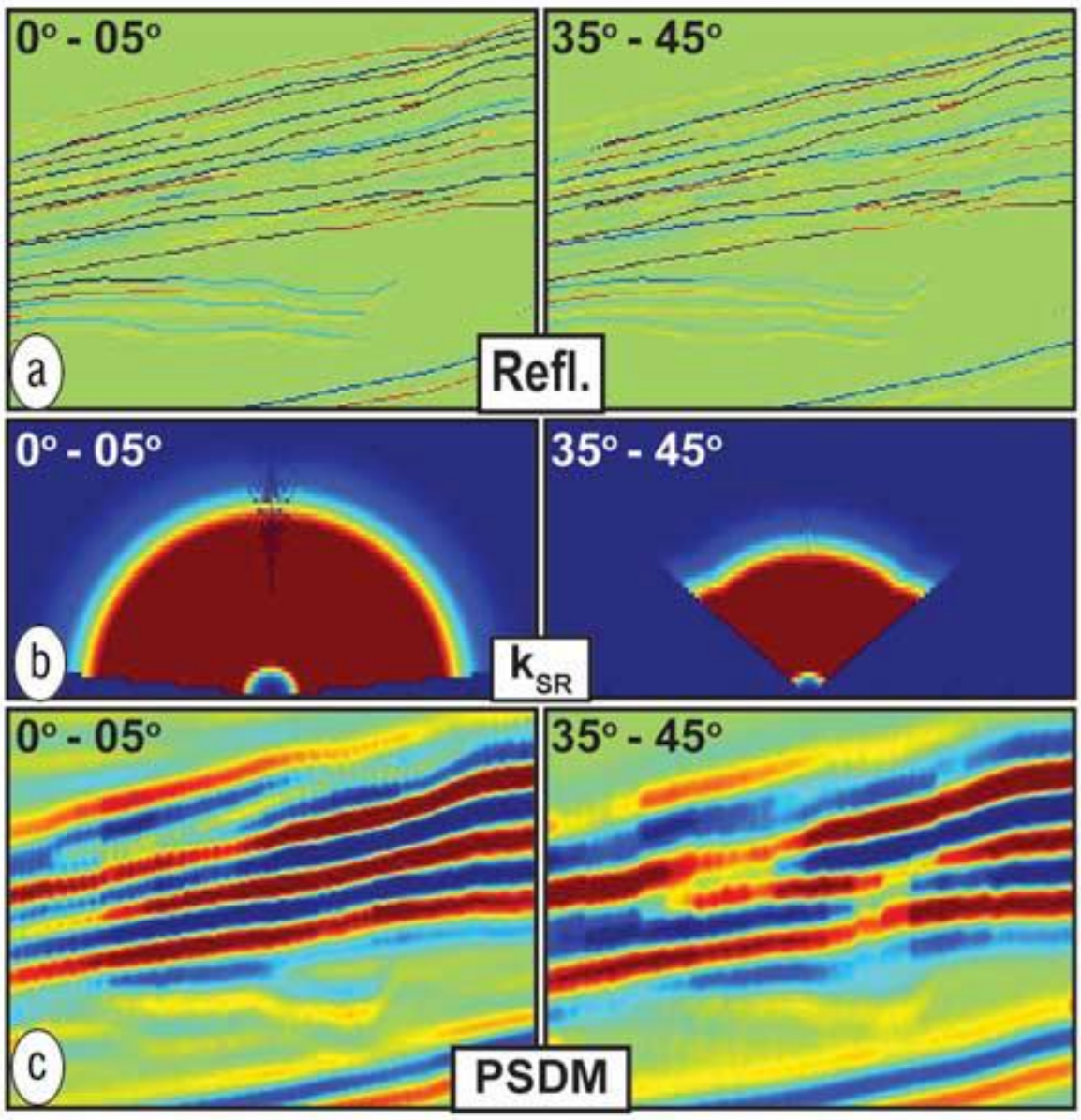

Figure 4.2: The effect of low angles of incidence (left) and high angles of incidence (right) on a) reflectivity, b) illumination, and c) resulting PSDM (Lecomte, 2008)

Elastic properties

The elastic properties of the model are used to simulate the facies present in the subsurface. A facies does not have a set value for each elastic property but can have a range of values depending on the composition of the facies in question. In order to determine how the detection rate of dolomite is affected by a variation in its elastic properties, four cases have been generated with varying values for the elastic properties (see table 4.1).

The four cases include low, original, high, and contrast. The differences between the first three cases are the properties of the dolomites in the model. For the "low" case, the dolomite's lowest value has been used for V_P, V_S, and ρ (Oldenburg D. et al., 2017), resulting in the lowest acoustic impedance. For the "original" case, the properties from field measurements of the HFF block have been used (H. J. Corlett et al., 2018). In the "high" case, the highest values for dolomite have been used (Oldenburg D. et al., 2017). For the "contrast" case, the elastic properties of the other facies are reduced by 10% while using the highest values for dolomite. This attribute reduction results in a case where no reflectors have the same strength as any of the possible dolomite reflectors, which will be further explored in section 4.4.

Model	**V_P [m/s]**	**V_S [m/s]**	**Density [kg/m3]**	**source**	**average V [m/s]**
Original	6254	3575	2560	(Schön, 2015)	5500
Low	5095	3178	2500	(Oldenburg et al., 2017)	5500
High	6500	3600	2840	(Oldenburg et al., 2017)	5500
Contrast*	6500	3600	2840	(Oldenburg et al., 2017)	5500

Table 4.1: Dolomite elastic properties. The contrast model uses the "high" values and reduces the elastic properties of all other facies.

4.3.1 Frequency

The frequency variable in the PSF-based convolution modeling refers to the frequency used to generate the used Ricker wavelet. The frequency variable used to generate the Ricker wavelet is also the dominant frequency of the wavelet, which can be used to correlate the synthetic cases to real-life cases. Higher frequencies attenuate at a higher rate than lower frequencies, which mean

that high-frequency signals will have less penetration depth than lower frequencies and will be lost for deeper prospects. This attenuation is not considered in the PSF-based convolution method but can be implemented using a more complex code with raytracing. However, a clear effect for the synthetic seismic data is how the resolution changes with wavelength. A signal's wavelength is inversely proportional to its frequency (see formula 4.2).

$$\lambda = \frac{v}{f}$$

Formula 4.2: Wavelength as a function of frequency

The horizontal and vertical resolutions depend on the signal's wavelength; a longer wavelength will result in a lower resolution. The vertical resolution is directly proportional to the wavelength and is based on the Rayleigh criterion. The Reyleigh criterion states that two waves are just distinguishable if the peak of one wave lies directly above the trough the other wave (Urone & Hinrichs, 2018). The horizontal resolution is more complex than the vertical as it varies due to how the signal is focused. A receiver will receive signals from an area where constructive interference occurs instead of the signal from a point. This area is called the first Fresnel zone, and its radius is a good measurement for horizontal resolution before it is migrated. The formulas for both resolutions are given below, where r_V is the vertical resolution, r_H is the horizontal resolution, λ is the wavelength, and z is the depth (Geldart & Sheriff, 2004).

4.3.2 Illumination

The illumination angle is the maximum dip of the substrata that can be illuminated. If a stratum dips too steeply, the reflected signal will not be recorded on the surface because it is not within the recording aperture and will, therefore, not show up on the seismic image. The illumination angle is dependent on the illumination vector. In a seismic survey, the illumination vector bisects the incident slowness vector and the reflected slowness vector for each shot and receiver pair. The illumination vector indicates which reflectors are illuminated, i.e., all reflectors with a normal-vector parallel to an illumination vector will appear on seismic (Lecomte, 2008).

In the PSF-based convolution modeling, the illumination angle is a variable used to control which reflector dips will be imaged in reality. Figure 4.3 gives an example of surfaces that will be illuminated (in green) and surfaces that are too steep (in red) according to the selected illumination angle value. On earth, the illumination angle depends on several factors, including the overburden and the acquisition-survey geometry. However, the modeling here does not relate to a specific overburden and survey, so the illumination angle is a more straightforward parameter used to reproduce limited realistic illumination effects (Lecomte, 2008).

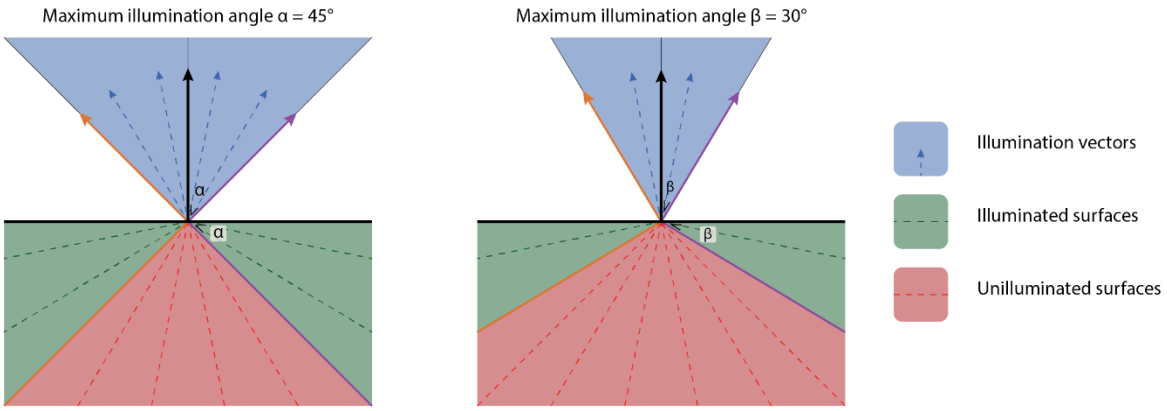

Figure 4.3: Illumination angle, surfaces in the green range are illuminated, and the surfaces in the red range are too steep to be illuminated and will, therefore, not show up on the seismic image

4.3.3 Angle of Incidence

The angle of incidence is the angle at which the ray incidents the horizon (see figure 4.4). This angle is usually the same as the reflection angle, but as mentioned in section 4.3.2, it is not

necessarily the case. An increase in the angle of incidence causes a reduction in the illumination angle and the reflectivity (Lecomte, 2008).

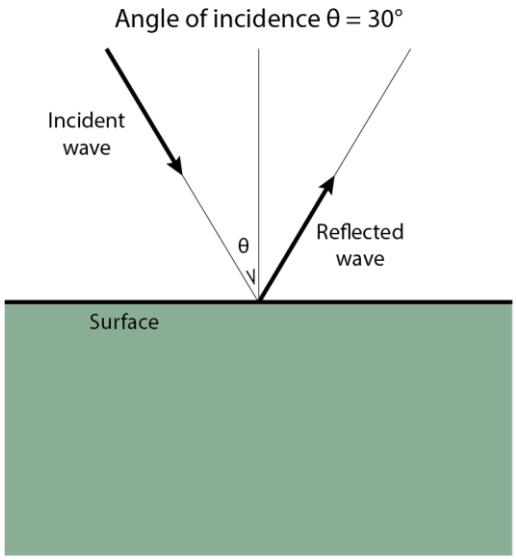

Figure 4.4: Angle of incidence is the angle at which the P and S waves incident the reflective surface.

4.3.4 Seismic data

The data to be analyzed in this thesis are the seismic data generated from the selected settings and attributes mentioned above in section 4.3. The resulting seismic cubes of the different cases will be analyzed individually. The seismic cubes will be visually compared by extracting time and horizon slices. The seismic cubes will be analytically compared by how much of the dolomite can be interpreted. The methods for dolomite recognition will be discussed later in this chapter.

4.3.5 The geometry of the model

The geometry of the model, its layers, and the elastic properties of the lithologies that are not dolomite are kept constant (see table 4.2) to be able to compare the results of the different cases directly. The geometry is made to simulate the HFF block, an analog for the subsurface of the Gulf of Suez. The Gulf of Suez contains multiple oil and gas fields in their production stage (*Egypt Concession Map,* 2022), which means that the HFF block has a high chance of containing reservoir-quality rock.

Facies	V_P [m/s]	V_S [m/s]	Density [kg/m3]
Conglomerate	5233	3117	2540
Packstone with grainstone	5095	3178	2500
Wackestone	3718	2437	2550
Mudstone	3718	2437	2550
Grainstone	4465	3038	2250
Clast supported conglomerate	5350	2950	2650
Channel grainstone	5137	3417	2530
Fining upward	5253	3190	2540
Breccia	5233	3117	2540
Esna formation	3850	2550	2440
Sudr formation	3510	2300	2380
Matulla formation	3470	1800	2360
Volcanic	6300	1860	2400
Massive N & S	5795	3371	2610

Table 4.2: Facies' elastic property values, the contrast case increases all of these values by 10% (He & Schmitt, 2006; Schön, 2011, 2015; Fabricius et al., 2008; Smallwood and Maresh, 2002; Elvebakk, H., 2010; Martinez et al., 2006)

4.3.6 The wavelet used

For this thesis, the Ricker wavelet is used. Other wavelets were considered, but due to the popularity of the Ricker wavelet, much information is available about it; this makes the Ricker wavelet a safe choice when comparing the impact of other attributes (Gholamy & Kreinovich, 2014).

Eleven cases have been created with different parameter settings to analyze the effect of each parameter (see table 4.3). These cases have been created so that each parameter is altered individually to isolate their effect, with one exception. The illumination angle and the angle of incidence have been altered as a pair.

Case	Model	Frequency	Wavelet	Illumination angle	Incident angle
1	Original	30Hz	Ricker	0-45°	0°
2	Original	60Hz	Ricker	0-45°	0°
3	Original	90Hz	Ricker	0-45°	0°
4	Original	30Hz	Ricker	0-25°	15°
5	Original	30Hz	Ricker	0-15°	25°
6	Low	30Hz	Ricker	0-45°	0°
7	High	30Hz	Ricker	0-45°	0°
8	Contrast	30Hz	Ricker	0-45°	0°
9	Low	30Hz	Ricker	0-15°	25°
10	High	30Hz	Ricker	0-15°	25°
11	Contrast	30Hz	Ricker	0-15°	25°

Table 4.3: Synthetic seismic settings

4.4 Reflectors

The model selected for this thesis is complex but realistic, with frequent variation in lithology both vertically and laterally. Due to the many different lithologies, and the fact that most of them occur throughout the entire model, there are many transitions in acoustic impedance, resulting in many possible seismic responses in the Lower Thebes Formation (see table 4.4). There are boundaries with reflectivities that could indicate a transition with dolomite. These similar boundaries have been counted for each case (see table 4.5). Note that conglomerate and breccia, as well as wackestone and mudstone, have identical values for velocity and density, which have therefore

been grouped. Dolomites and massive dolomites are two separate entities. Since the massive dolomites are not the subject of this thesis, they were not evaluated.

The reflection coefficient (R) of the boundary between two layers can be described based on the acoustic impedance (Z) of the two layers (see formula 3.4). Layer 1 is the lower layer, and layer 2 is the upper layer, with the wave propagating through the upper layer. The acoustic impedance is based on the elastic properties of the layer (see formula 3.3); the bulk density ρ, and the velocity V (Simm & Bacon, 2014). Note that the reflectivity can be calculated separately for P and S waves using their respective velocities.

	Co/Br	Pa	Wa/Mu	Gr	Cl	Fi
Conglomerate /Breccia	0.00	0.02	0.17	0.14	-0.03	0.00
Packastone	-0.02	0.00	0.15	0.12	-0.05	-0.02
Wackestone /Mudstone	-0.17	-0.15	0.00	-0.03	-0.20	-0.17
Grainstone	-0.14	-0.12	0.03	0.00	-0.17	-0.14
Clast supported	0.03	0.05	0.20	0.17	0.00	0.03
Fining upward	0.00	0.02	0.17	0.14	-0.03	0.00
Dolomite	0.09	0.11	0.26	0.23	0.06	0.09

Table 4.4: Reflectivity of lithological boundaries for the "original" elastic properties. The incident medium is along the horizontal axis, and the reflective medium is along the vertical axis. The table assumes that the incident angle is 0. Dolomite-generated reflections are represented in dark green, and reflectors that could be mistaken for dolomite are represented in light green.

Reflectivity	**Dolomite**		**Other facies**		**Confusing results**	
Cases	**min**	**max**	**min**	**max**	**lower**	**similar**
Low	-0.15	0.05	-0.2	0.2	36	24
Original	-0.26	-0.06	-0.2	0.2	8	8
High	-0.32	-0.13	-0.2	0.2	7	7
Contrast	-0.41	-0.23	-0.2	0.2	0	0

Table 4.5: Reflectivity ranges for the dolomites and other facies as reflecting layers. The number of results that might be confused for dolomite is listed out of 36 possible reflectivities. The "lower" category counts cases with a lower reflectivity than the highest reflectivity of dolomite. The "similar" category counts cases within the dolomite reflectivity range.

The upper Thebes Formation includes all lithologies except clast supported, breccia, and dolomites. The lower Thebes Formation includes all lithologies except channel grainstones. Important to note here is that the massive dolomite deposits are only present in a very small area of the model, which means that the accompanying high change in acoustic impedance does not perpetrate throughout the upper Thebes Formation. In addition, the channel grainstones are only present in the bottom-most part of the upper Thebes Formation, which means that there are transitions between channel grainstones and the lithologies specific to the Lower Thebes Formation.

4.5 Statistical Analysis

In order to determine how the model variables affect the ability to interpret dolomite deposits, a statistical analysis has to be performed. The statistical analysis allows the direct comparison of the results when the variables mentioned above in section 4.4 are changed.

4.5.1 The binary downscaling method

The binary downscaling method refers here to the downscaling of an RMS or model surface, but instead of the common practice of averaging the values, it produces a binary version based on the threshold chosen. From here on out, the method will be referred to as “downscaling”. A lower threshold will yield more positive results due to the process's nature, which will affect the confusion matrix values described below. The initial threshold value was based on a visual assessment. The threshold that would produce a downscaled version most resembling the original surface was used; 8%.

A python script has been created for the statistical analysis of the results. The script’s input is a black-and-white image of the attribute surface generated in Petrel, as well as color-coded images of the actual locations of dolomite at the appropriate surfaces, which can be extracted from the model.

The images have been post-processed in Photoshop to ensure that all the images are aligned and scaled equally and that only the accepted color codes are present. See appendix 2 for the entire script with instructions on the process.

First, the script divides the images into a grid with equal elements based on a downscaling factor, a factor of 1:50 turns 50x50 pixels into one element. The script then separates the elements into "hits" and "misses" based on the element's contents. A cell from the model will be considered a hit if the amount of dolomite exceeds the threshold value, while a cell from the synthetic seismic will be considered a hit if the amount of high amplitude pixels exceeds the dolomite threshold value. What constitutes a high amplitude pixel is based on the autoscaling scale bar in Petrel and differs for each of the cases (see table 4.6). If the same cut-off value were selected for all the cases, several of them would have been exclusively above or below the threshold as the parameters shift the RMS amplitude range.

	Case 1	**Case 2**	**Case 3**	**Case 4**	**Case 5**	**Case 6**	**Case 7**	**Case 8**	**Case 9**	**Case 10**	**Case 11**
Cut-off	0.095	0.115	0.125	0.067	0.045	0.058	0.125	0.165	0.045	0.058	0.080

Table 4.6: cut-off values for what constitutes a potential dolomite indicator

The size of the grid elements created when downscaling the images can be calculated using the scales and number of pixels present in the original images. The pixels/km ratio can be determined and used to calculate the grid size of all the scales generated by the script (see table 4.7)

Scale	**length of pixel side**
1:200	2.94 km
1:100	1.47 km
1:50	0.73 km
1:25	0.37 km
1:10	0.15 km
1:5	0.08 km
1:1	0.02 km

Table 4.7: scale factors and corresponding grid sizes

For the script to properly work, the file names must be precisely formulated as follows: "case_vv_black _white_co_xxx_freq_yy_Qzz_Illu_ww" where letter combinations are replaced with information describing the attributes belonging to the downscaled images:

xxx = the three digits after the "0." of the cut-off point between black and white for the RMS amplitude

yy = The frequency of the seismic used

zz = the horizon or part of horizon used (either c for complete, t for thin, or s for small)

ww = the illumination angle of the seismic used

vv = the case as described in the materials and methods chapter

4.5.2 Confusion matrix

A confusion matrix is a 2 x 2 matrix with a "true" class on one axis and a "predicted" class on the other axis (see figure 4.5). Both classes can be true or false; the four resulting outcomes are true positive, true negative, false positive, and false negative.

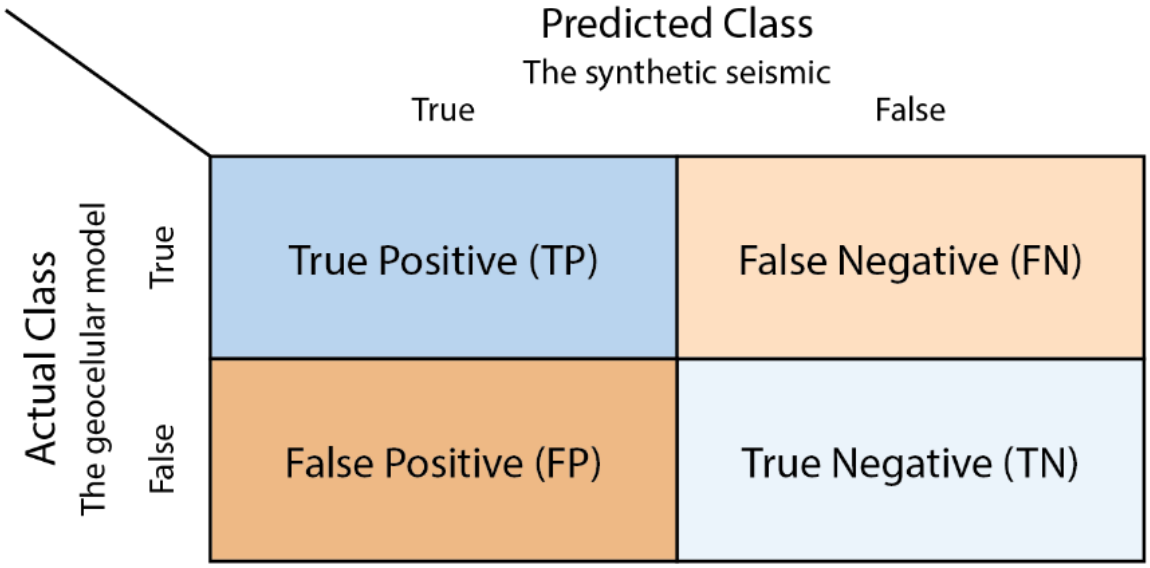

Figure 4.5: A confusion matrix (Demir, 2022)

The four elements of a confusion matrix:

- A true positive value is a correct prediction of a dolomite presence. The model shows that there is a dolomite "hit," and the RMS amplitude predicts a dolomite "hit."

- A true negative is a correct prediction that there is no dolomite presence. The model shows that there is no dolomite, and the RMS amplitude correctly predicts this.
- A false positive is an incorrect prediction that there is a dolomite presence. The model shows that there is no dolomite, but the RMS amplitude predicts that there is dolomite.
- A false negative is an incorrect prediction that there is no dolomite presence. The model shows that there is dolomite, but the RMS amplitude fails to predict its presence.

The confusion matrix can be used to calculate many different performance metrics. Sensitivity measures how much of the actual class's true part was correctly predicted, while specificity measures how much of the actual class's false part was correctly predicted. A decrease in the threshold of the downscaling method will result in more positive values increasing the number of true positives and false positives, thereby increasing the sensitivity but decreasing the specificity. Depending on the purpose, there will be a desired sweet spot between the specificity and sensitivity, which can be found by changing the threshold. In this thesis, another performance metric is used instead; Matthew's Correlation Coefficient.

4.4.3 Matthew's correlation coefficient

Also known as the Yule phi coefficient, Matthew's Correlation Coefficient (MCC) is a coefficient that describes the relationship between a prediction and the actual values. The coefficient uses the four variables, true positive, false positive, true negative, and false negative, and returns a value between -1 and 1 (see formula 4.3). A 0 indicates no correlation between the prediction and the actual values, while a 1 and -1 indicate a perfect correlation and a perfect inverse correlation, respectively (Chicco & Jurman, 2020).

$$MCC = \frac{TN \cdot TP - FN \cdot FP}{\sqrt{(TP + FP) \cdot (TP + FN) \cdot (TN + FP) \cdot (TN + FN)}}$$

Formula 4.3: Calculation for Matthew's correlation coefficient (Chicco & Jurman, 2020)

The MCC is used here instead of other performance metrics for the confusion matrix because the MCC weighs all the available results instead of just a subset of the four available outcomes, as is the case in the accuracy or F1 score (Chicco & Jurman, 2020).

4.4.4 Permutation testing of the MCC against random results

In order to prove that the RMS amplitude map can be used to predict dolomite geobodies, a relationship must be established between the two. Since a relationship cannot be directly proven, a null hypothesis must be formulated and disproven.

The null hypothesis: The RMS amplitude cannot be distinguished from a randomly generated RMS amplitude map when its resemblance to dolomite occurrences is calculated.

In order to disprove this null hypothesis, a permutation test can be performed. In this permutation test, the number of hits and misses from the downscaled RMS amplitude surface are reorganized randomly. The randomized surface is then compared to the downscaled model surface to produce an MCC as a performance metric. The MCC values are recorded and used to determine a probability curve of MCC values representing random RMS amplitude maps. The original observed MCC is then compared to the probability curve; if the p-value of the observed MCC is under 0.005, the null hypothesis is disproven. If the null hypothesis is disproven, the relationship is established, and it is proven that the RMS amplitude map can be used to predict dolomite occurrences.

During the thesis, two issues have been encountered related to the MCC.

The first issue is a division by 0 error created due to how the MCC is calculated, and this error occurs in 4 specific circumstances. Whenever the true class or the predicted class only consists of 1 value, either all true or all false, the MCC will result in a division by 0 error. During the analysis, this error has occurred on multiple occasions, especially when the dolomite threshold is set too high, as the predicted class will never generate a “True”. These errors have been counted as insignificant results as the code fails to make a prediction.

The second issue with the MCC is a binning artifact caused by the fact that only a certain number of unique results are possible with each set combination of “True” and “False”, causing problems when plotting the histograms for the permutation test. Multiple solutions have been tried, but if two of these unique values are too close, it will result in a spike twice as high as it should be or a

missing bin (see figure 4.6). About 40% of the histograms suffer from it each time the script is executed. This issue is only a visual one, and the data is unaffected, which can be concluded from the fact that the issue disappears or appears randomly on subsequent runs with a different number of bins and does not affect the percentile values. The issue can be fixed by manually plotting each bin, but it will likely be a very time-consuming fix for a visual issue. The choice has been made to address the issue here and only use graphs that do not suffer from this issue elsewhere in the thesis. Because of the explicit randomization used, the normal distribution will still behave like a randomly generated distribution.

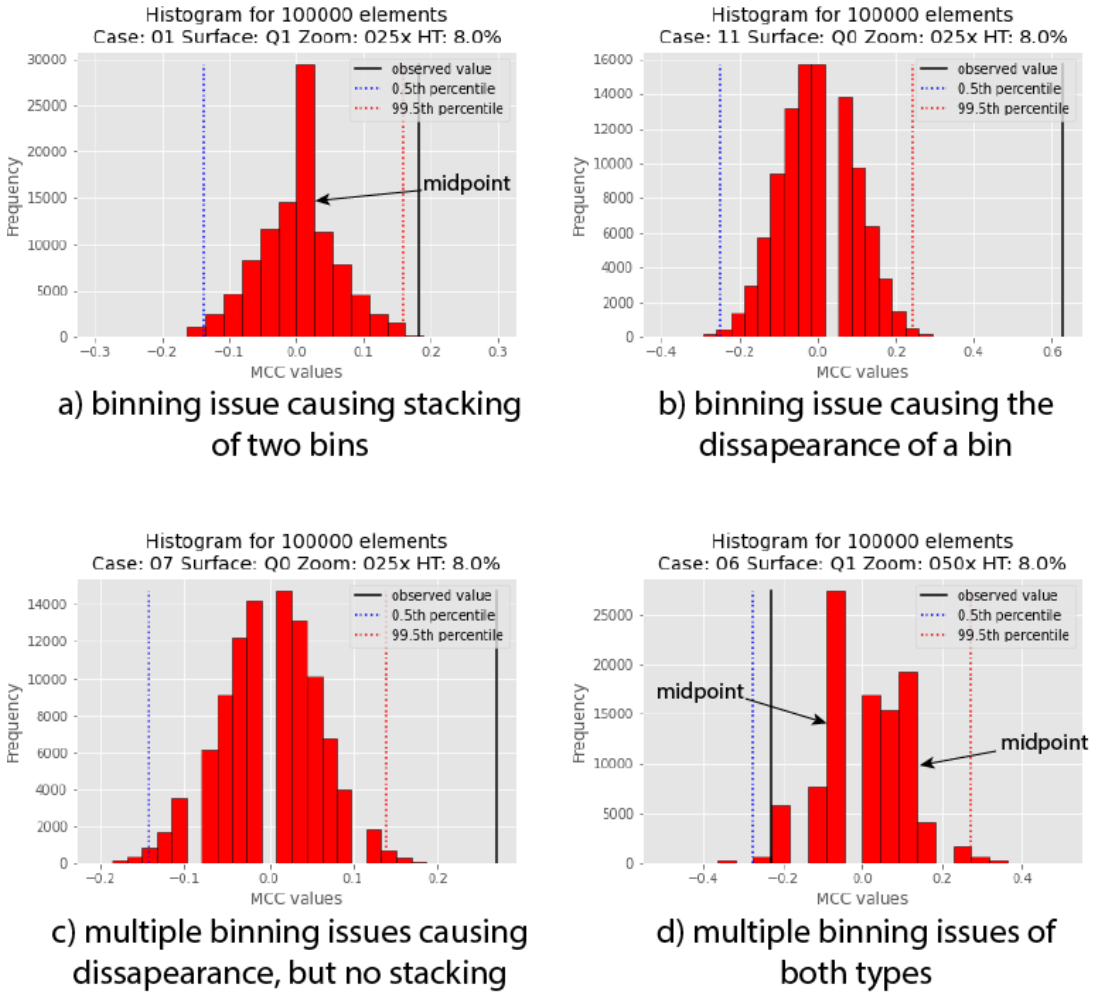

Figure 4.6 Visual binning errors in the histograms. Two possible binning errors, apparent summation of 2 bins and the disappearance of a bin. It is also possible for multiple of one to occur or multiple of both.

An issue with the method

While creating the attribute surfaces for the model, a surface had to be chosen. The problem with creating own interpreted surfaces is that the vast number of lithological transitions makes it almost impossible to pinpoint the boundary between the Upper and Lower Thebes Formation despite the clear differences in the 3D model view.

The model included surfaces along which the cells where ordered. These cells, however, do not correspond to the boundaries of the different lithologies modeled and would not likely be a surface interpreted by geologists. These surfaces were selected as horizons for both the RMS amplitude and model surfaces.

When creating the seismic interpretation for the attribute horizons, an additional issue occurs for the 90Hz cases; the increase in resolution is so high that the individual cells of the geocellular model become visible, introducing a step-like effect to the reflectors (see figure 4.7). This step-like effect can be seen as stripes on the RMS amplitude map (see figure 4.8).

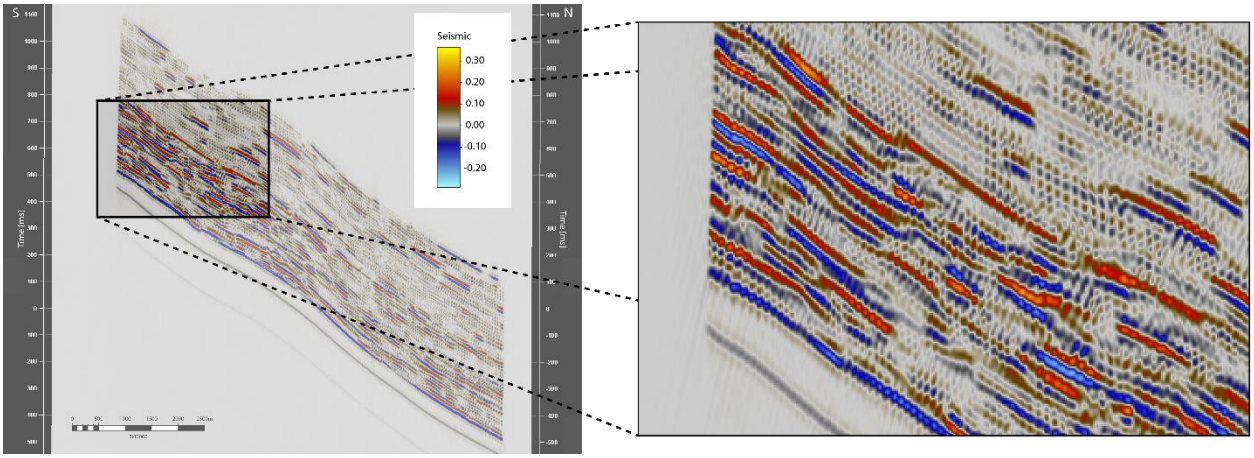

Figure 4.7 Inline 401 of the synthetic seismic of case 3 (90Hz) zoomed, suffers from an aliasing effect. Increase in impedance gives a positive response and is dispayed in red.

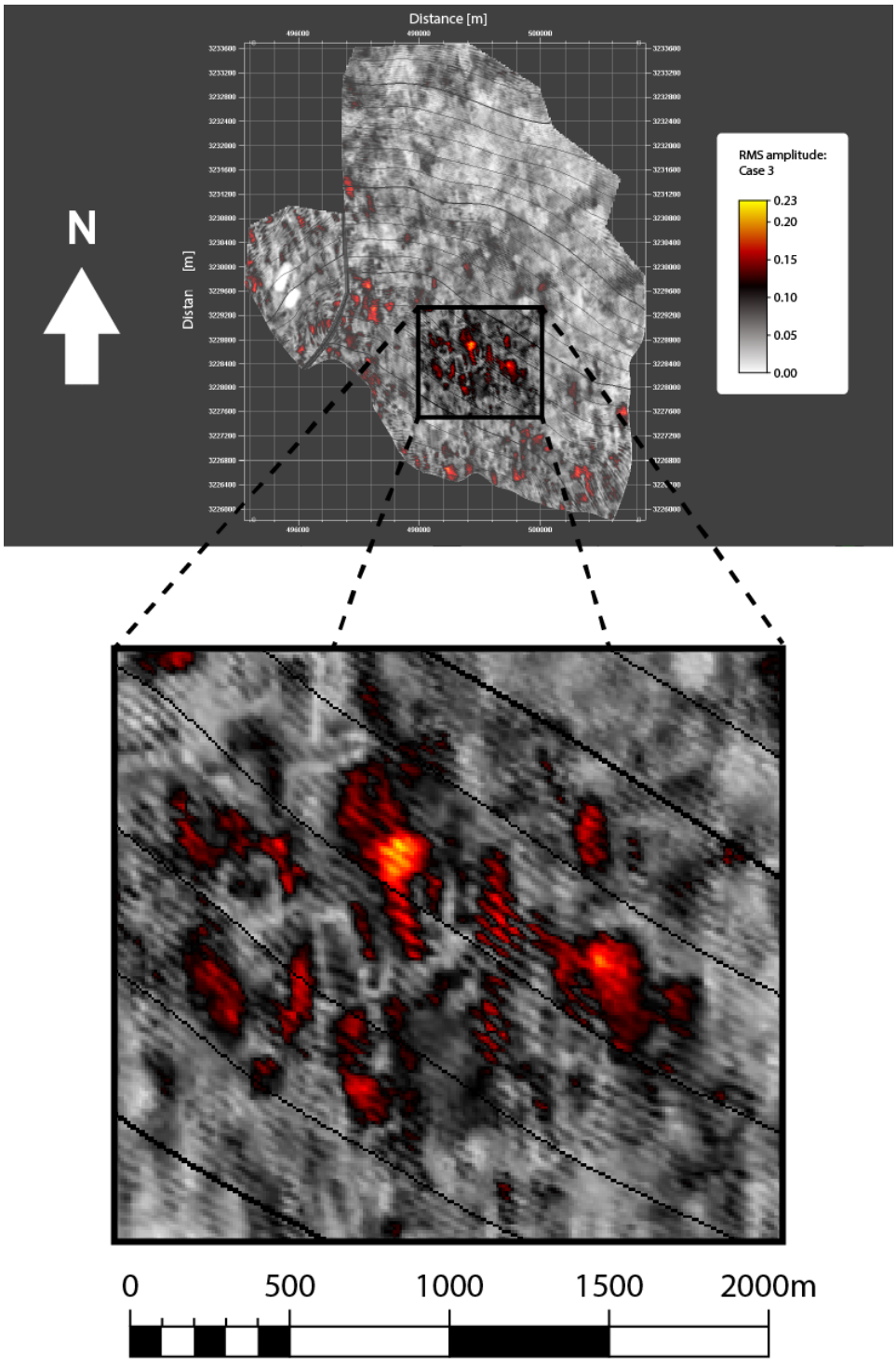

Figure 4.8 RMS atribute surface Q2 of case 3. The aliasing issue caused by the high frequency is clearly visible as NW-SE stipes.

5 Results

5.1 Introduction

The main aim of this thesis is to determine the effect of several variables when gathering seismic data on the quality of the data gathered. The variables are simulated by the settings available in the PSF modeling software. The resemblance of the RMS amplitude attribute surface to the corresponding surface in the model is used as a performance metric of the predictive capabilities of the seismic. The factors that will be analyzed in this chapter are the signal frequency, the illumination angle and incidence angle, and the elastic properties of the dolomite to be identified.

The data needed to analyze these effects is gathered using PSF modeling software to generate a synthetic seismic, and seismic exploration and production software was used to generate RMS amplitude attribute surfaces. The attribute surfaces were generated along five surfaces in the area of interest, the Lower Thebes Formation. The attribute surfaces and corresponding model surfaces were then downscaled at several scales. The downscaled model and attribute surface were compared using Matthew's correlation coefficient after it was normalized to remove any artifacts introduced during the downscaling.

5.2 Observations

The model can visually be divided into two layers, the upper layer is dominated by grainstone and wackestone, and the lower layer is dominated by conglomerate and packstone with graystone (see figure 5.1). These are the layers described in chapter 4.1, the Upper Thebes Formation and the Lower Thebes Formation. Dolomite (in brown) only occurs in the Lower Thebes Formation and only in the southern part of the model along the modeled equivalent of the Hammam Faraun Fault (see figure 5.1). The northern half of the model does not contain dolomite.

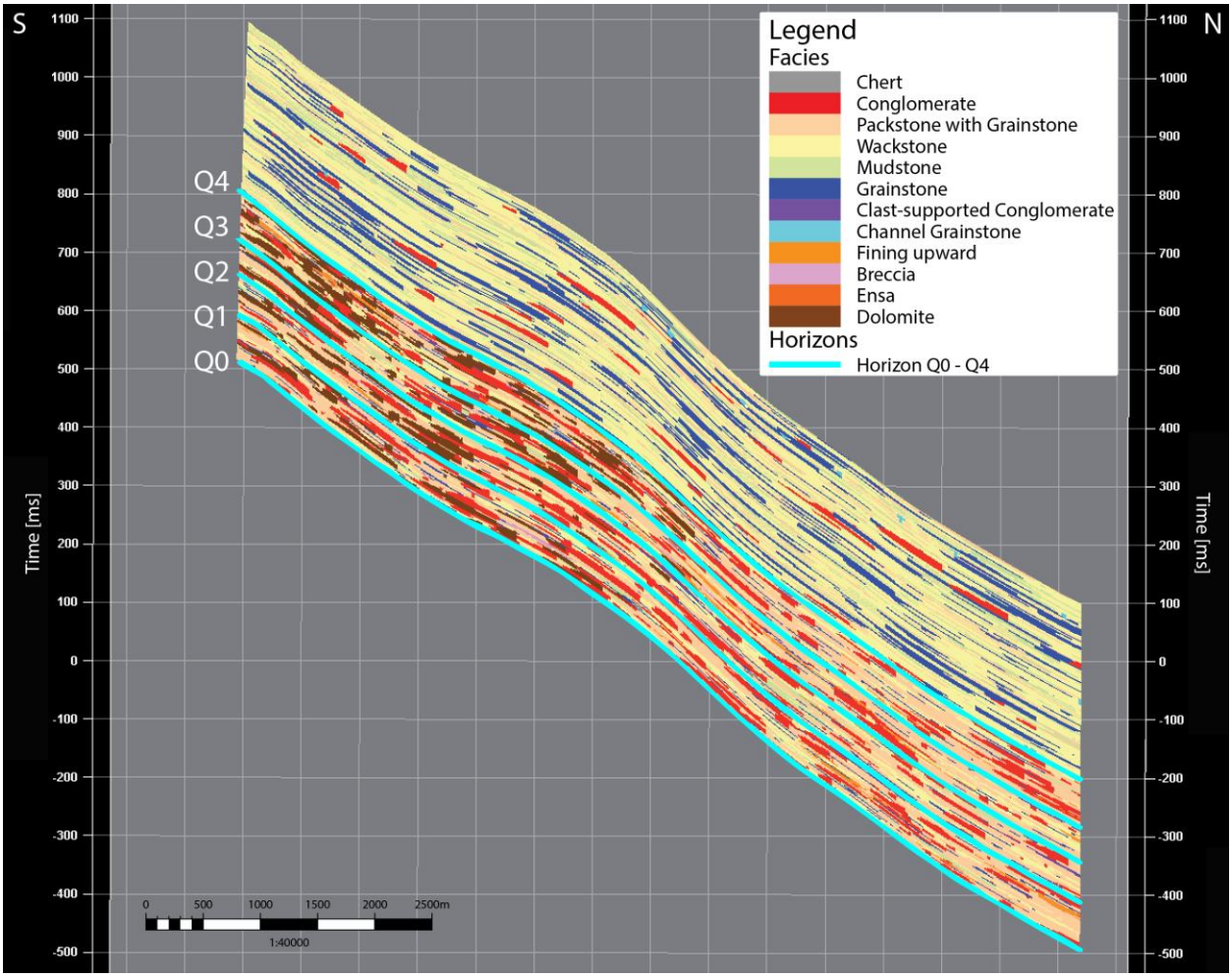

Figure 5.1: Dolomites (in brown) as present in the model displayed on inline 401.

5.3 RMS amplitude

Five surfaces have been selected to analyze the dolomites in the Lower Thebes Formation. The surfaces (Q0 – Q4) have been selected equidistant throughout the Lower Thebes Formation, with the upper and lower surfaces being the upper and lower boundary of the Lower Thebes Formation (see figure 5.1). An RMS amplitude map was generated for all five surfaces using a 30ms interval around the horizon, 15ms above to 15ms below. The 30ms interval was chosen to include the thickness of 1 seismic reflector on a 30Hz seismic trace. This RMS amplitude map has been generated for each of the 11 cases. The RMS amplitude surfaces for case 1 are shown, as well as a case 11 surface to show the difference in model size used when changing the illumination angle. The change is necesarry because of the issue discribed in section 5.6.3 (see figure 5.2).

The actual dolomite occurrences, as defined by the model, have been overlaid onto the RMS amplitude map (see figure 5.3). From the resulting image can be observed that the RMS amplitude peaks are mainly located in the western and southern sections of the model, with a few peaks in the middle and north as well (see figure 5.3). The actual dolomite deposits are in the south and west, following a trend similar to the RMS amplitude peaks; this indicates a possible relationship between the two. However, there is no dolomite in the middle or north of the model. When looking at a zoomed-in image, the RMS amplitude peaks sometimes coincide with dolomite occurrences, but other times they do not (see figure 5.4). In order to determine whether the observed trend in the RMS amplitude data is significant or whether it could have been a random coincidence, a permutation test has been performed (as described in section 4.5). Since the data matches poorly on a small scale (see figure 5.4), the downscaling method (see section 4.5) has been applied to the permutation test to analyze whether this method will help analyze larger-scale trends.

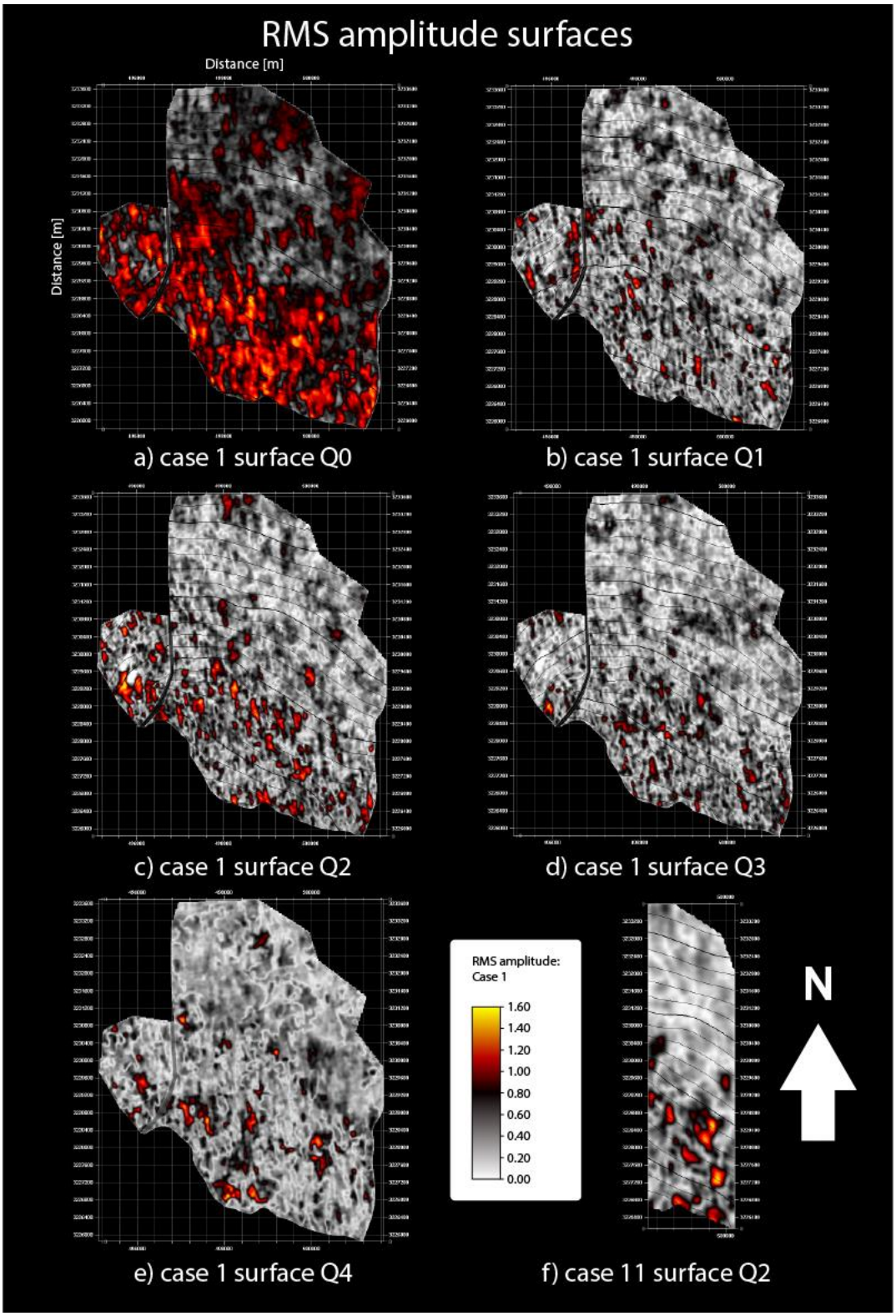

Figure 5.2: Dolomites and RMS amplitude peaks for surfaces of case 1 and surface Q2 for case 11

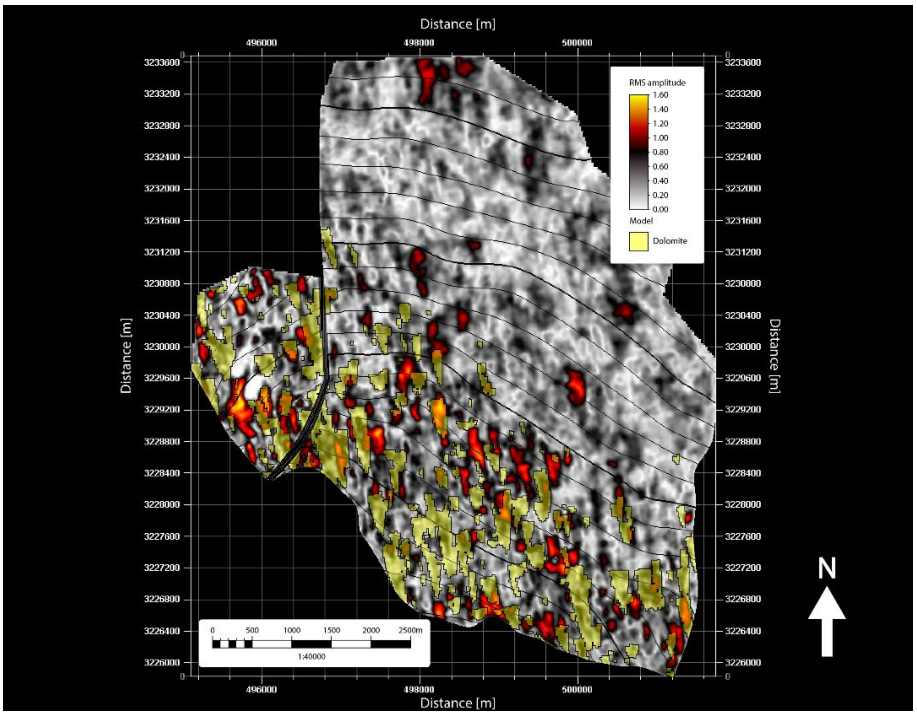

Figure 5.3: Dolomites and RMS amplitude peaks for case 1 on surface Q2

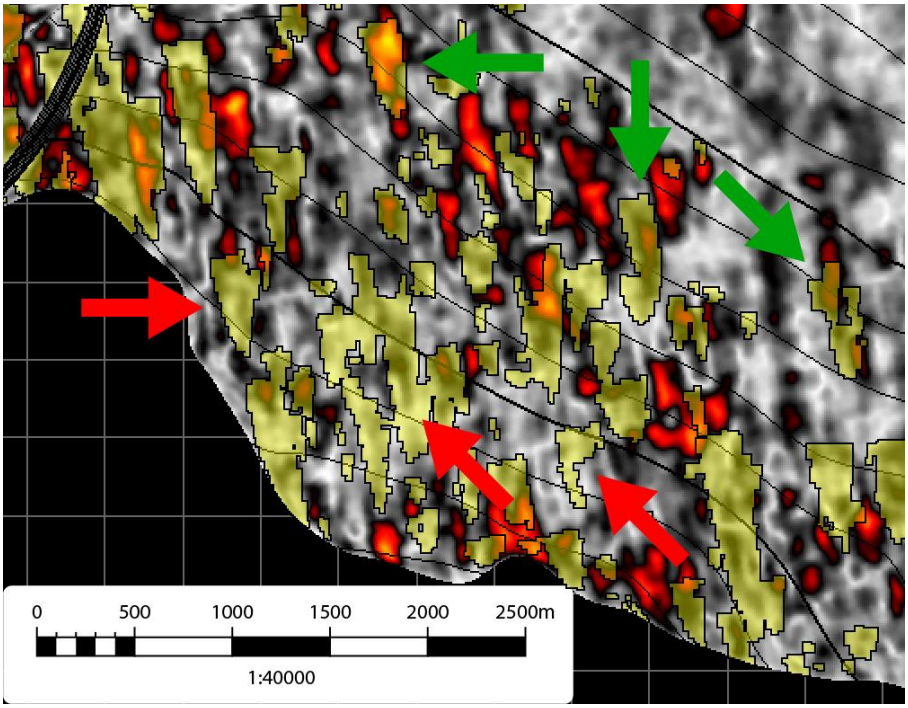

Figure 5.4: Dolomites and RMS amplitude peaks for case 1 on surfaces Q2, peak matches labeled green, mismatches labeled red (not extensive)

5.4 Downscaling method

In order to analytically find a correlation between the large-scale trend that the RMS amplitude and the model share, the downscaling method was created expressly for this thesis. The downscaling method was created to analyze trends that occur on different scales to highlight the large-scale correlation observed between the model's dolomite and the RMS amplitude's peaks (see figure 5.4). A workflow of the downscaling method has been visualized (see figures 5.5, 5.6, and 5.7). The image will be divided into a grid where each grid element is colored white for a dolomite presence or black for a dolomite absence. In order to constitute a dolomite presence, a threshold value has to be met. The standard has been set to 8% (by area). This threshold is varied throughout the data collection to analyze its effect on the predictive capabilities of the RMS amplitude. These elements with a dolomite presence will be referred to as "hits" going forward. When both the model and the RMS amplitude have been gridded, the grids are compared, and four outcomes are counted, the true positives, true negatives, false positives, and false negatives. These values are used to calculate Matthew's Correlation Coefficient (MCC), a measurement of the resemblance between the two images.

The four elements of a confusion matrix (Chicco & Jurman, 2020):

- A true positive value is a correct prediction of a dolomite presence. The model shows that there is a dolomite "hit," and the RMS amplitude predicts a dolomite "hit."
- A true negative is a correct prediction that there is no dolomite presence. The model shows that there is no dolomite, and the RMS amplitude correctly predicts this.
- A false positive is an incorrect prediction that there is a dolomite presence. The model shows that there is no dolomite, but the RMS amplitude predicts that there is dolomite.
- A false negative is an incorrect prediction that there is no dolomite presence. The model shows that there is dolomite, but the RMS amplitude fails to predict its presence.

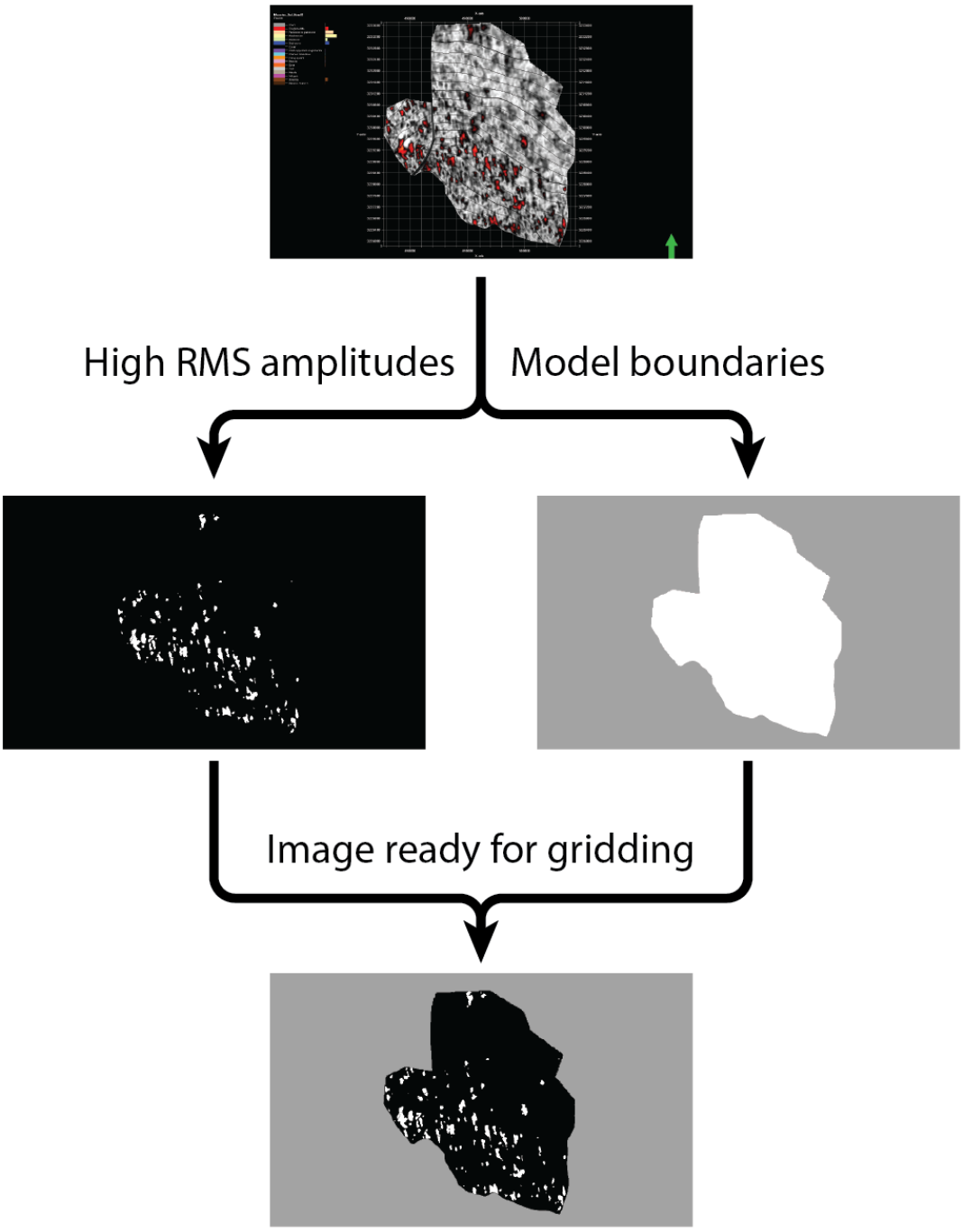

Figure 5.5: Preparing the image for gridding.

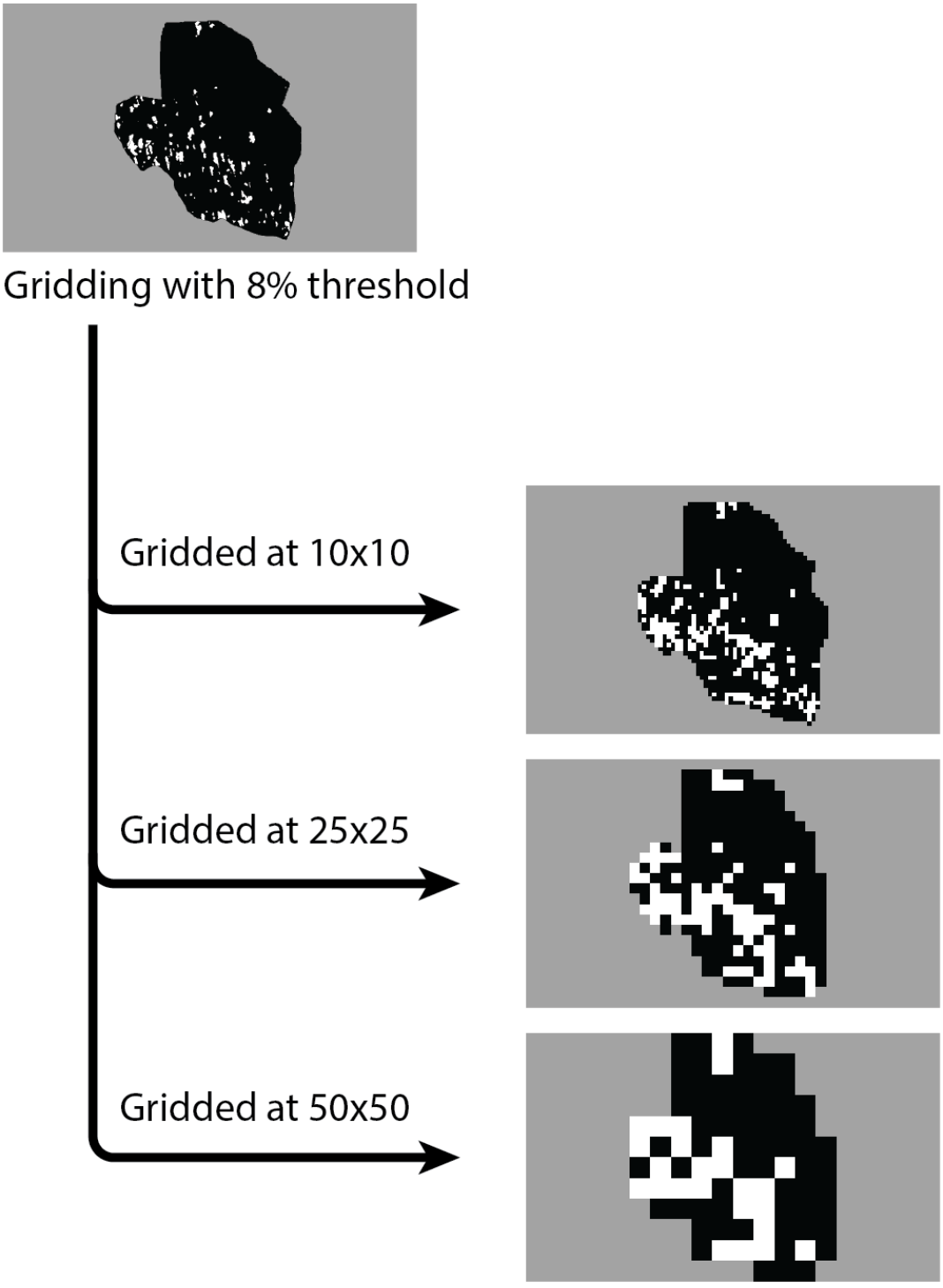

Figure 5.6: Gridding the image at different scales.

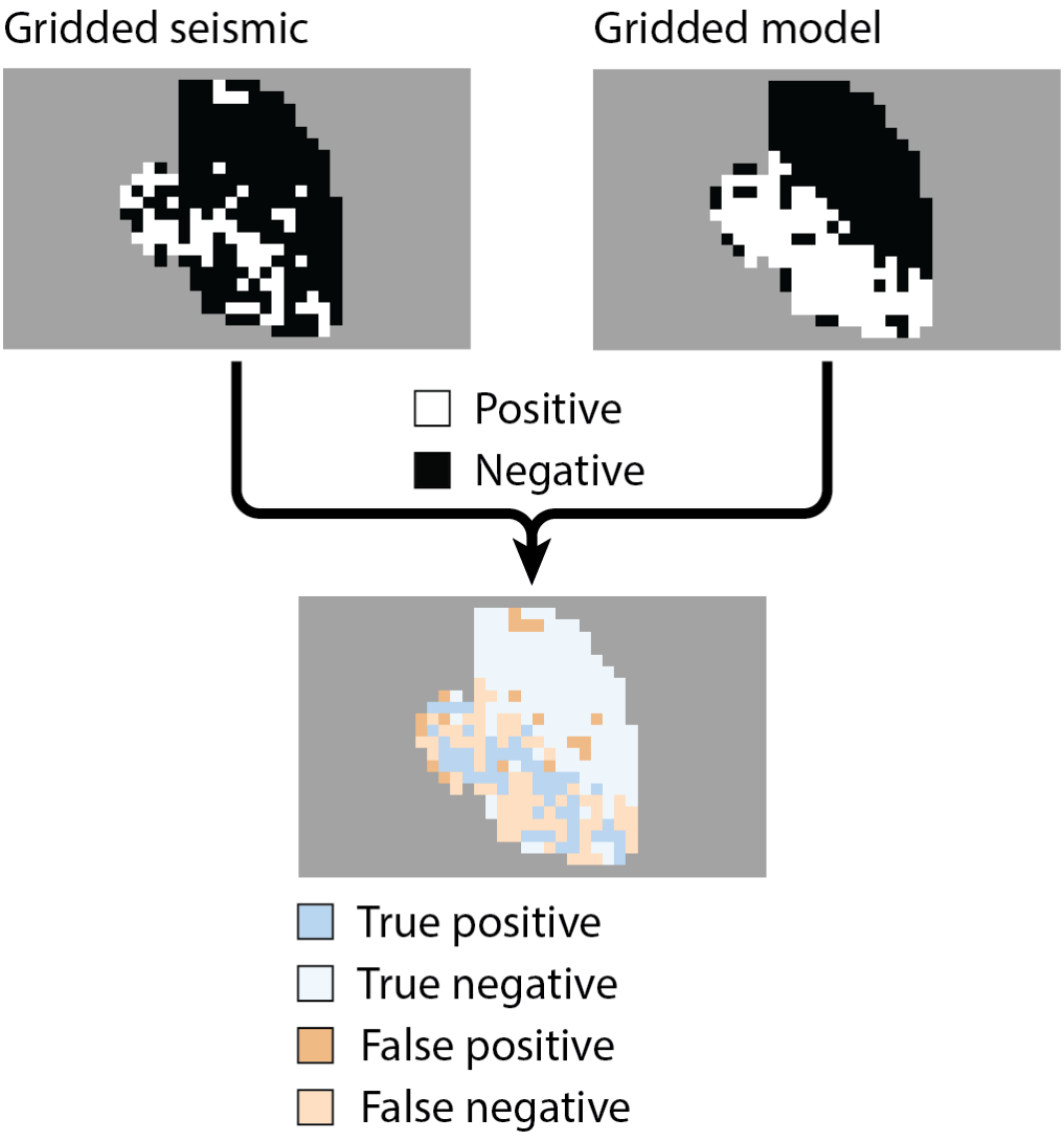

Figure 5.7: Determining the confusion matrix values of the gridded seismic based on the gridded model for each image and scale.

I created the downscaling method used in this thesis to force clarity in the conclusion. The RMS amplitude scale generated by Petrel was used to select the boundary between dolomite predictions (white) and no prediction (black). As the upper and lower boundaries vary from case to case, the

value for the selected point varies, resulting in different cut-off points for the cases (see table 5.1). If a static cut-off value had been chosen, several images would have been entirely black or white.

The downscaling method takes inspiration from a mosaic image consisting of smaller images. When zoomed in, the exact data points seem dissociated and separate images, but a bigger picture appears when zooming out.

	Case 1	**Case 2**	**Case 3**	**Case 4**	**Case 5**	**Case 6**	**Case 7**	**Case 8**	**Case 9**	**Case 10**	**Case 11**
Cut-off	0.095	0.115	0.125	0.067	0.045	0.058	0.125	0.165	0.045	0.058	0.080

Table 5.1: cut-off values for what constitutes a potential dolomite indicator

5.5 Statistical analysis

The MCC generated using the gridded RMS amplitude and model surface is a performance metric of the resemblance between the two and can therefore be used to measure how well the RMS amplitude map predicts the dolomite occurrences. The MCC ranges from -1 to 1, where 1 is a total resemblance, 0 is the worst, and -1 is a completely inverted resemblance. A -1 and 1 are equally good results in this case, as a -1 does predict the exact locations but assesses the wrong attribute as a positive indicator (Chicco & Jurman, 2020).

In order to determine whether the MCCs generated are significant compared to a randomly generated result, a permutation test can be applied to the result. The permutation test generates 100000 random gridded images and calculates the MCC for each of them with regard to the model surface. If the probability of the observed MCC randomly occurring is less than 0.5% (a p-value of 0.005), the MCC will be determined as significant (see figure 5.8). If the probability is higher, the observed MCC is deemed insignificant (see figure 5.9). The positively significant and negatively significant values were calculated but tallied separately; this is, therefore, a bi-sided test, meaning that both results can be analyzed separately (Chen et al., 2019).

When calculating the 99.5^{th} percentile for the different cases, a clear trend with regard to the scale of the grid can be observed. A large-scale map (see figure 5.8) has a lower threshold for values to

become significant (around 0.15), while a small-scale map (see figure 5.9) has a higher threshold for significance (around 0.3). This is likely an artifact of the downscaling process, and to analyze the MCC data correctly, it has to be normalized with regard to the significance threshold (the 99.5^{th} percentile). The MCC values have been normalized by subtracting the 99.5^{th} percentile from the MCC.

In order to determine the performance of different cases, surfaces, and grid scales, the number of significant results produced by each case have been counted and compared (see tables 5.2, 5.3, and 5.4). This number of significant results does not represent how closely the prediction (RMS amplitude) matches the actual scenario (the model), but it represents how often a significant prediction is made. The normalized MCC values have been plotted to analyze the seismic data quality and how well it can be used to make predictions, i.e., how closely it resembles the truth (the model) (see figure 5.10).

Some data points result in the division by zero error that occurs when either the true class (the model) or the predicted class (the RMS amplitude attribute map) have only true or only false values (see section 4.5). These values are counted as insignificant results in the analysis and will affect the success rates for the cases and parameter variables.

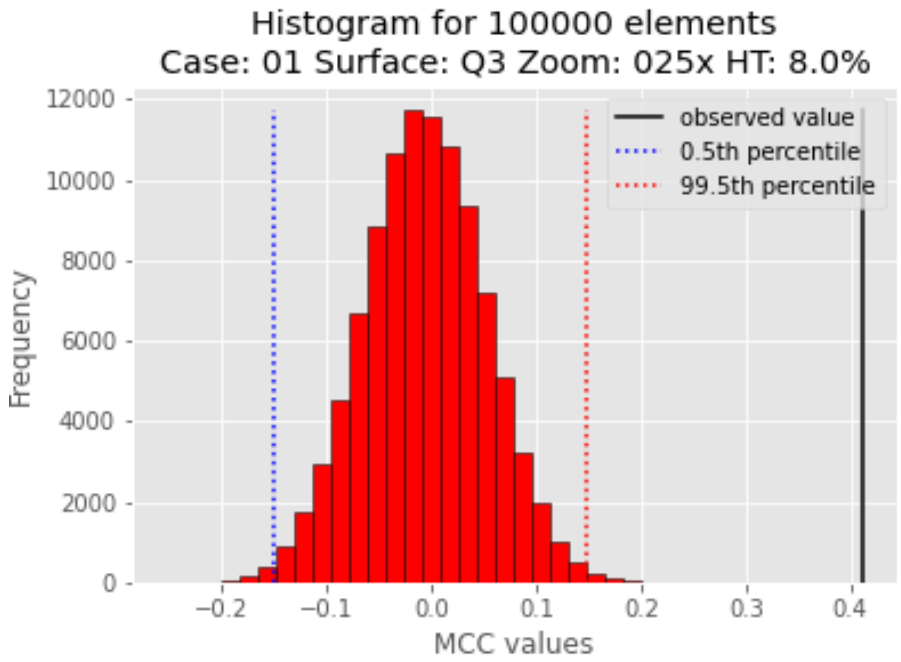

Figure 5.8: A permutation test for a significant result, the observed value is above the 99.5th percentile and will be counted as a positively significant result.

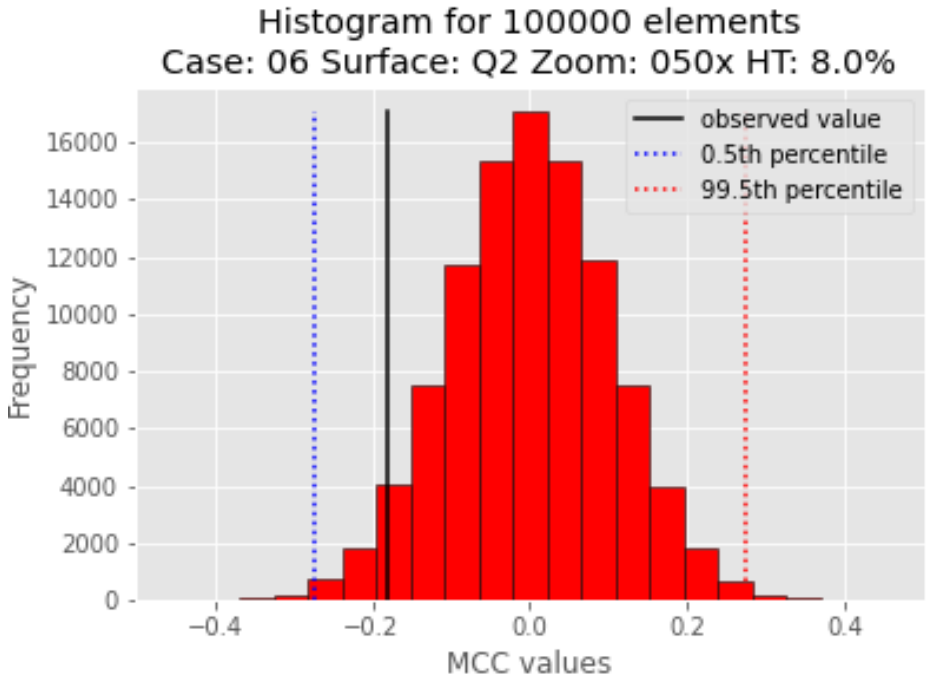

Figure 5.9: A permutation test for an insignificant data point, the observer value is below the 99.5th percentile and will be counted as a positively insignificant result.

Surface	Directly significant	Inversely significant	Total	Success rate (direct)
Q0	44	0	77	57%
Q1	31	0	77	40%
Q2	46	0	77	60%
Q3	45	0	77	58%
Q4	38	0	77	49%

Table 5.2: number of significant results for each surface (dolomite threshold 8%)

Case	Directly significant	Inversely significant	Total	Success rate (direct)
1	26	0	35	74%
2	27	0	35	77%
3	26	0	35	74%
4	12	1	35	34%
5	10	2	35	29%
6	2	13	35	6%
7	26	0	35	74%
8	29	0	35	83%
9	2	14	35	6%
10	20	0	35	57%
11	24	0	35	69%

Table 5.3: number of significant results for each case (dolomite threshold 8%)

Scale	Directly significant	Inversely significant	Total	Success rate (direct)
1:1	43	11	55	78%
1:5	43	8	55	78%
1:10	40	5	55	73%
1:25	37	4	55	67%
1:50	28	1	55	51%
1:100	13	1	55	24%
1:200	0	0	55	0%

Table 5.4: number of significant results for each scale factor (dolomite threshold 8%)

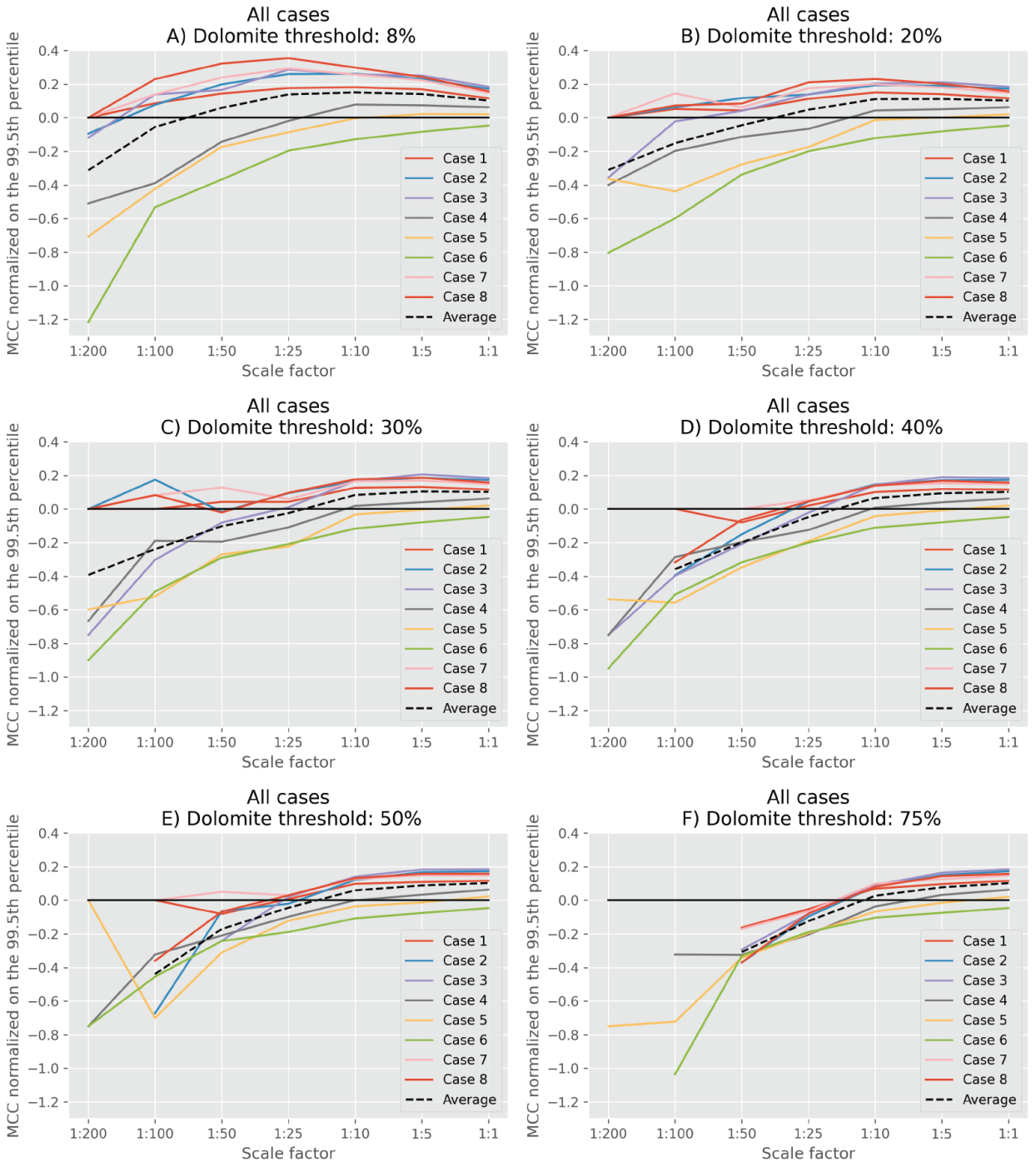

Figure 5.10: Trend in the significance of the data. MCC has been normalized on the 99.5th percentile and then plotted. Everything over y = 0 is a significant result. Higher values represent a more correct prediction. Dolomite threshold: a) 8% Dolomite b) 20% dolomite c) 30% Dolomite d) 40% dolomite e) 50% dolomite f) 75% dolomite.

5.6 Analysis by variables of interest

One of the main aims of this thesis is to analyze the effect of PSF modeling settings on the performance of dolomite prediction. The metric used to predict the presence of dolomite is the RMS amplitude map, and the way to assess the quality of the prediction is a normalized Matthews Correlation Coefficient. This section will analyze the effect of three variables on the prediction performance of dolomite. For each of the different analyses, a subset of the data has been selected to control all other variables (see table 5.5).

Variable of interest	**Cases used**
Frequency	Case 1, case 2, case 3
Illumination angle	Case 1, case 4, case 5
Elastic properties	Case 1, case 6, case 7, case 8

Table 5.5: Subset of data used to facilitate variable analysis

5.6.1 Changing the frequency

One of the main tested PSF settings is frequency. Here the effect of frequency on the ability to predict dolomite presences is analyzed. Cases 1, 2, and 3 vary only in the frequency used, and their results can therefore be used to analyze the frequency's effects on the prediction. For each of the 3 cases, 35 results are generated, one for each surface and scale factor combination. Some of these data points result in the division-by-zero error mentioned before (see section 4.5), which affects the MCC calculation; these are counted as insignificant values.

When comparing the synthetic seismic generated using 30Hz in case 1 (see figure 5.11) and using 90Hz in case 3 (see figure 5.12), it is clear that the reflected signal is thinner for a higher frequency (see figure 5.13). These thinner reflectors are due to the effect frequency has on the seismic resolution described in chapter 3.2.

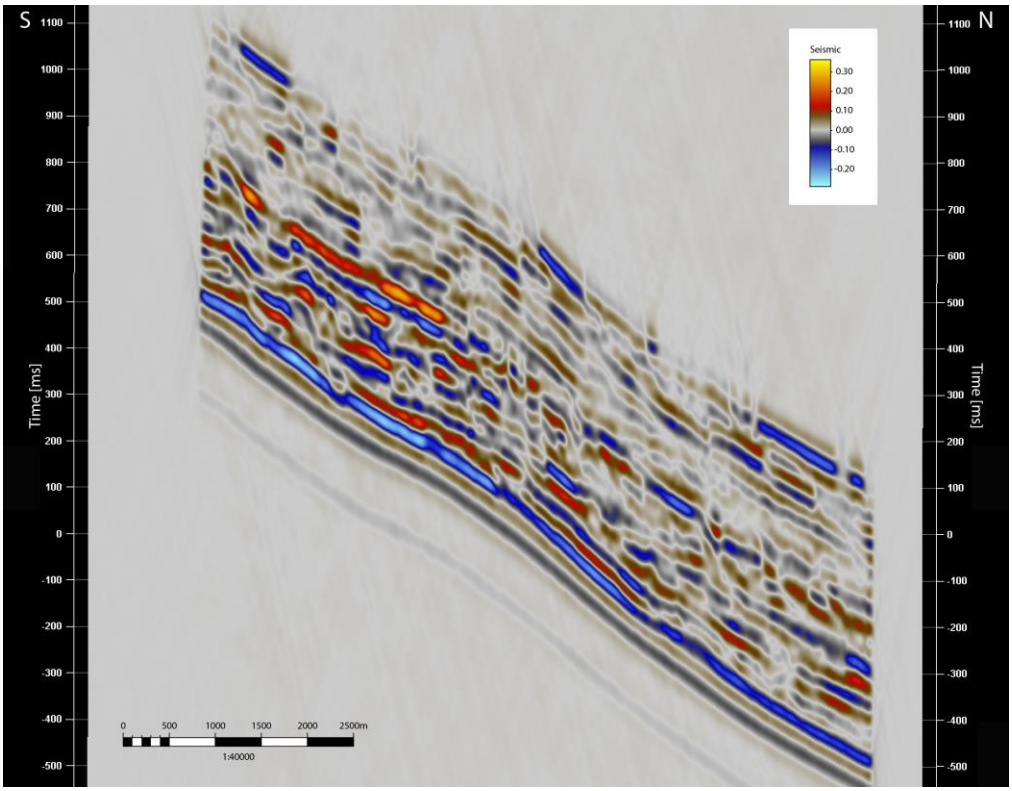

Figure 5.11 Inline 401 of the synthetic seismic 30Hz

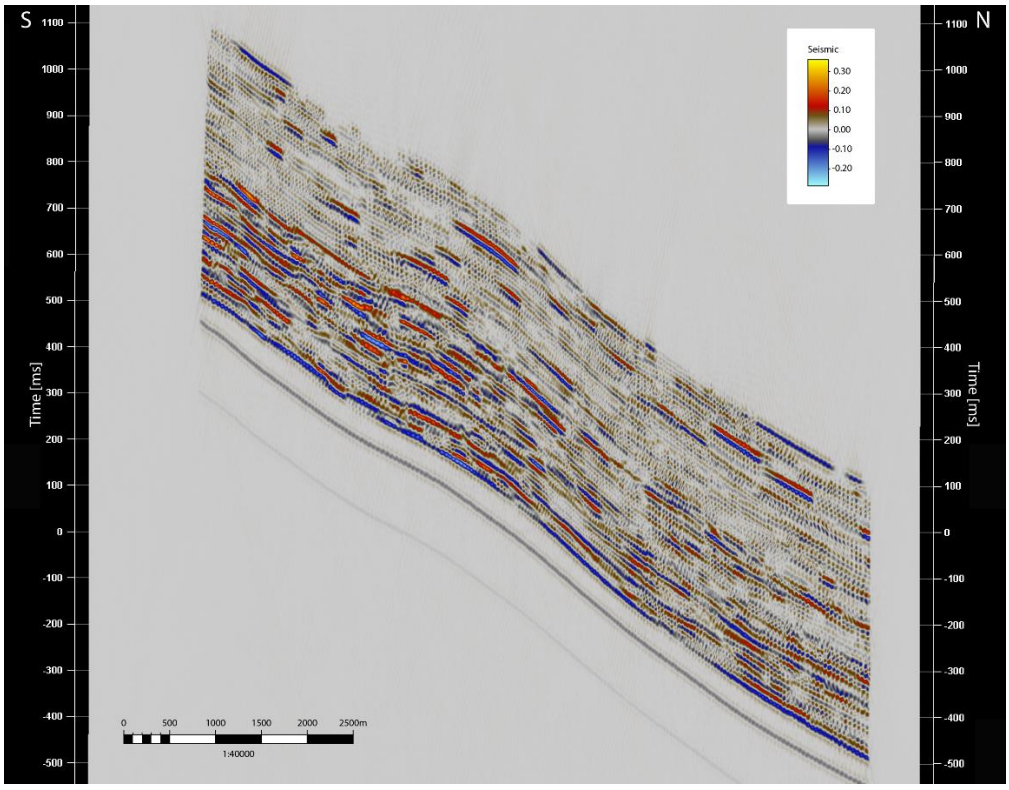

Figure 5.12 Inline 401 of the synthetic seismic 90Hz

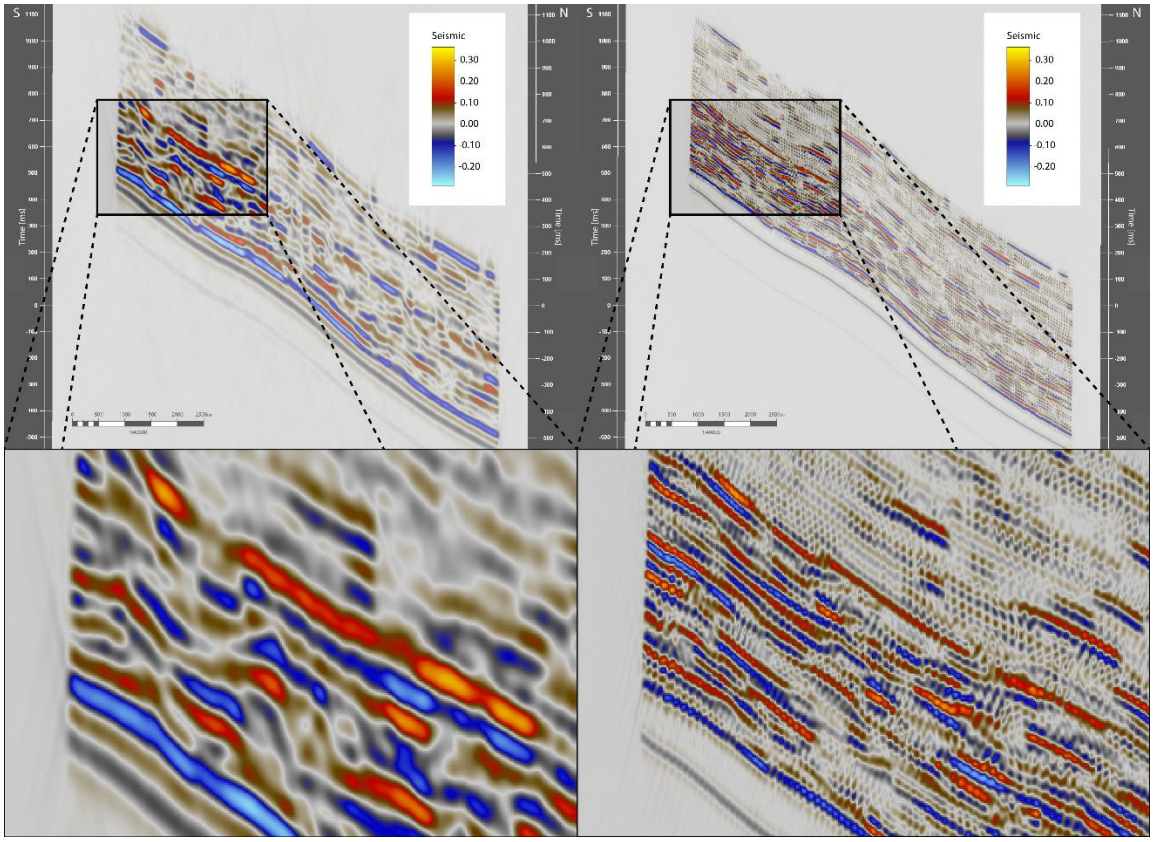

Figure 5.13 Inline 401 of the synthetic seismic zoomed, 30Hz left, 90Hz right. 90Hz shows many more reflectors than 30Hz. 90Hz suffers from an aliasing effect. Increase in impedance gives a positive response and is dispayed in red.

The number of significant results does not change based on the frequency (see table 5.6), but the result's significance changes depending on the frequency and scale factor (see figure 5.14). In order to visualize the significance of the different situations, the scale factor has been plotted against the chosen performance metric; the MCC normalized with regards to the 99.5th percentile (see figure 5.14). The average value of all five surfaces at the given frequency and scale factor have been used for the plot. The three data sets follow the same trend where the result is most significant around the 1:10 to 1:25 scale. The 60 and 90Hz cases are more significant than the 30Hz cases except for the 1:200 scale. The 90Hz average does not form a smooth trend, making it difficult to rate it compared to the 60Hz cases but placing it above the 30Hz cases. As the dolomite content required to constitute a hit increases, the lower scale factors behave more erratically, and the best predictive performance shifts towards higher scale factors. It is important to note that the 1:1 scale compares individual pixels and is, therefore, either 100% or 0% dolomite.

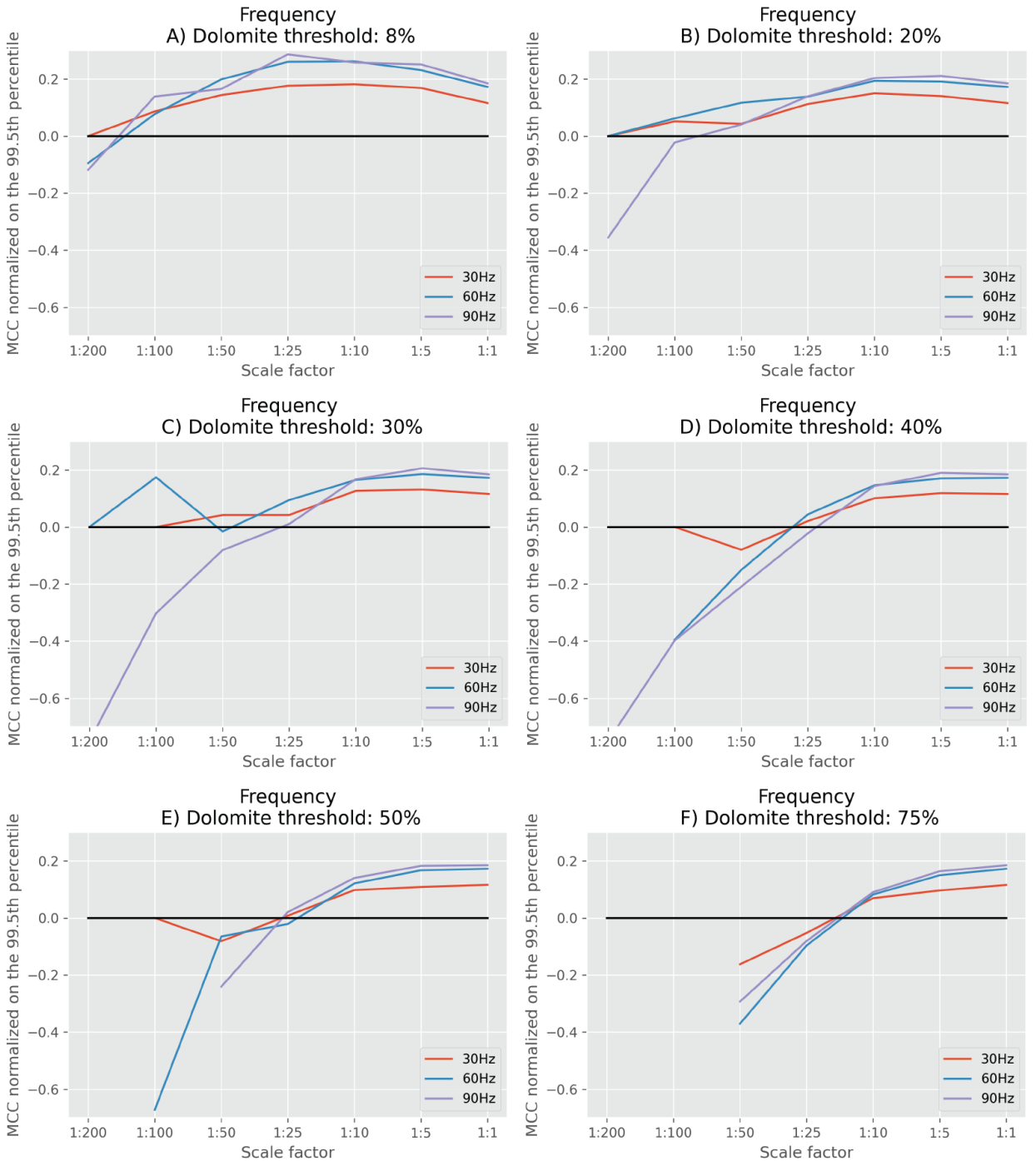

Figure 5.14: Trend in the significance of the frequency data. MCC has been normalized on the 99.5th percentile and then plotted. Everything over y = 0 is a significant result. Higher values represent a more correct prediction. Dolomite threshold: a) 8% Dolomite b) 20% dolomite c) 30% Dolomite d) 40% dolomite e) 50% dolomite f) 75% dolomite.

Case	Frequency	Directly significant	Inversely significant	Total	Success rate
1	30 Hz	26	0	33	79%
2	60 Hz	27	0	35	77%
3	90 Hz	26	0	34	76%

Table 5.6: The success rate of dolomite recognition by frequency (dolomite threshold 8%)

5.6.2 Changing the elastic properties

Dolomite is not a homogenous material, and the elastic properties will therefore differ throughout the geobodies. The difference in elastic properties will affect the acoustic impedance and, thereby, the seismic response. In order to analyze the effect on the synthetic seismic and the dolomite prediction, three additional models were created with different elastic properties and used to create cases 6, 7, and 8 (see figure 5.15). In order of elastic values, the cases are; low < original < high < contrast.

There is a general trend with regard to the success rate of the prediction; the higher the elastic properties are relative to the surrounding matrix, the more successful the prediction is. The prediction is more often successful (see table 5.7), and the predictions are more significant (see figure 5.15). The “Low” case does not result in any significant results since the elastic attributes for this case are in the same order of magnitude as the surrounding lithology and might, therefore, not show up on a seismic or RMS amplitude cube. Also, the higher hit threshold causes lower scale factors to produce more erratic data instead of following the expected trend. The lack of data points is caused by too many “division by zero” errors.

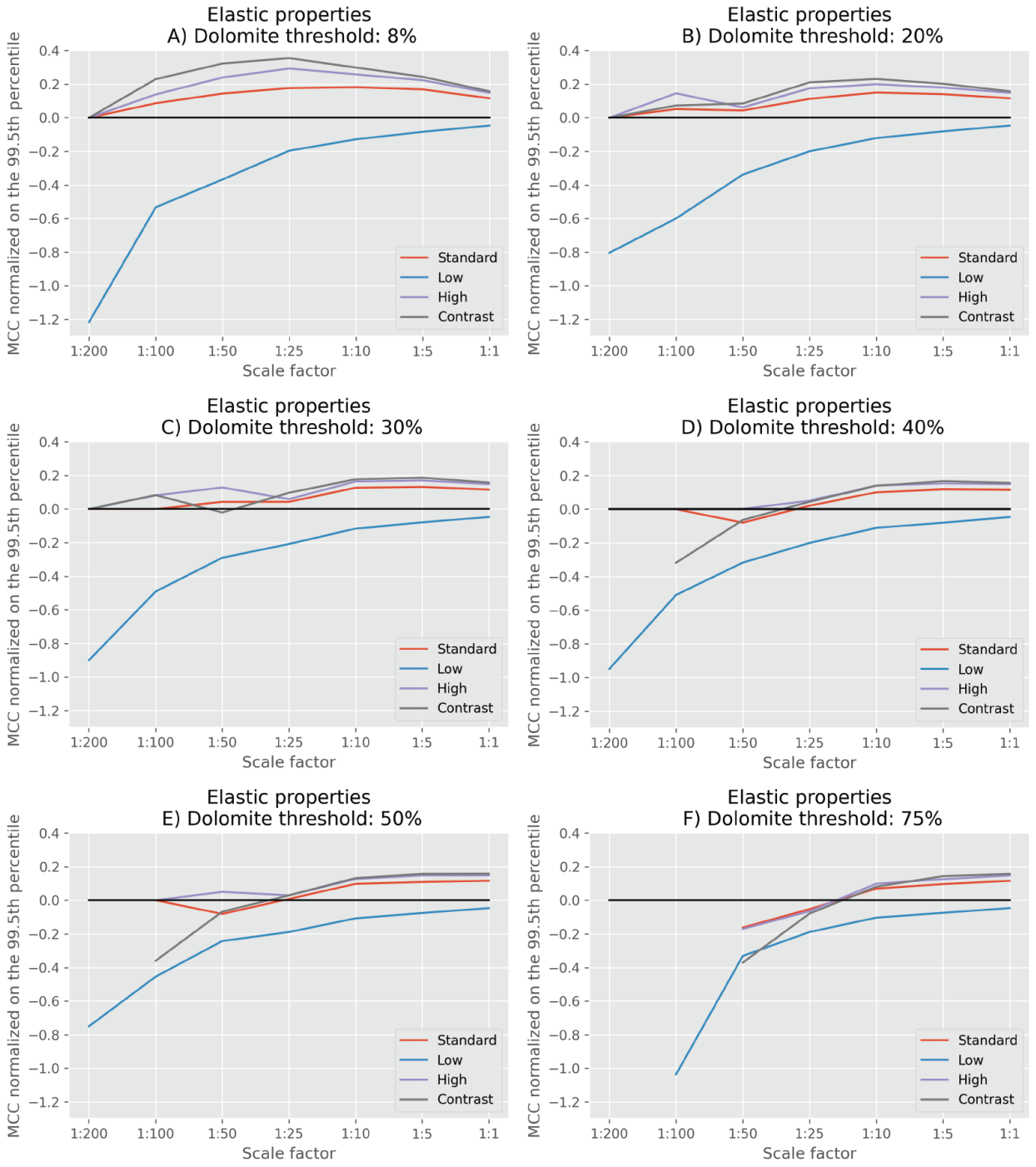

Figure 5.15: Trend in the significance of the elastic property data. MCC has been normalized on the 99.5th percentile and then plotted. Everything over y = 0 is a significant result. Higher values represent a more correct prediction. Dolomite threshold: a) 8% Dolomite b) 20% dolomite c) 30% Dolomite d) 40% dolomite e) 50% dolomite f) 75% dolomite.

Case	Properties	Directly significant	Inversely significant	Total	Success rate
1	Standard	26	0	33	79%
6	Low	2	13	32	0%
7	High	26	0	33	70%
8	Contrast	29	0	33	83%

Table 5.7: The success rate of dolomite recognition by elastic properties (dolomite threshold 8%)

5.6.3 Changing the Illumination

The third aspect of interest is the illumination and how it affects the dolomite indicators. Due to issues with the software used, it was impossible to generate a synthetic seismic for the complete model when altering the illumination and angle of incidence. Instead, a smaller target area has been generated. The selected area has been chosen to include the dolomite variation in the north-to-south direction. Due to the smaller sample size, the result may be more susceptible to random error, but it will be treated as equally valid for this thesis.

There is a general trend for the success rate; as the illumination angle increases, the success rate increases (see table 5.8). There is also a trend with regard to the significance of the results. The significance peaks at the 1:10 scale factor for 45° when a successful hit is determined as 8% dolomite in the grid (see figure 5.16.a). This peak shifts toward a higher scale factor as the dolomite amount required for a successful hit increases (see figure 5.16).

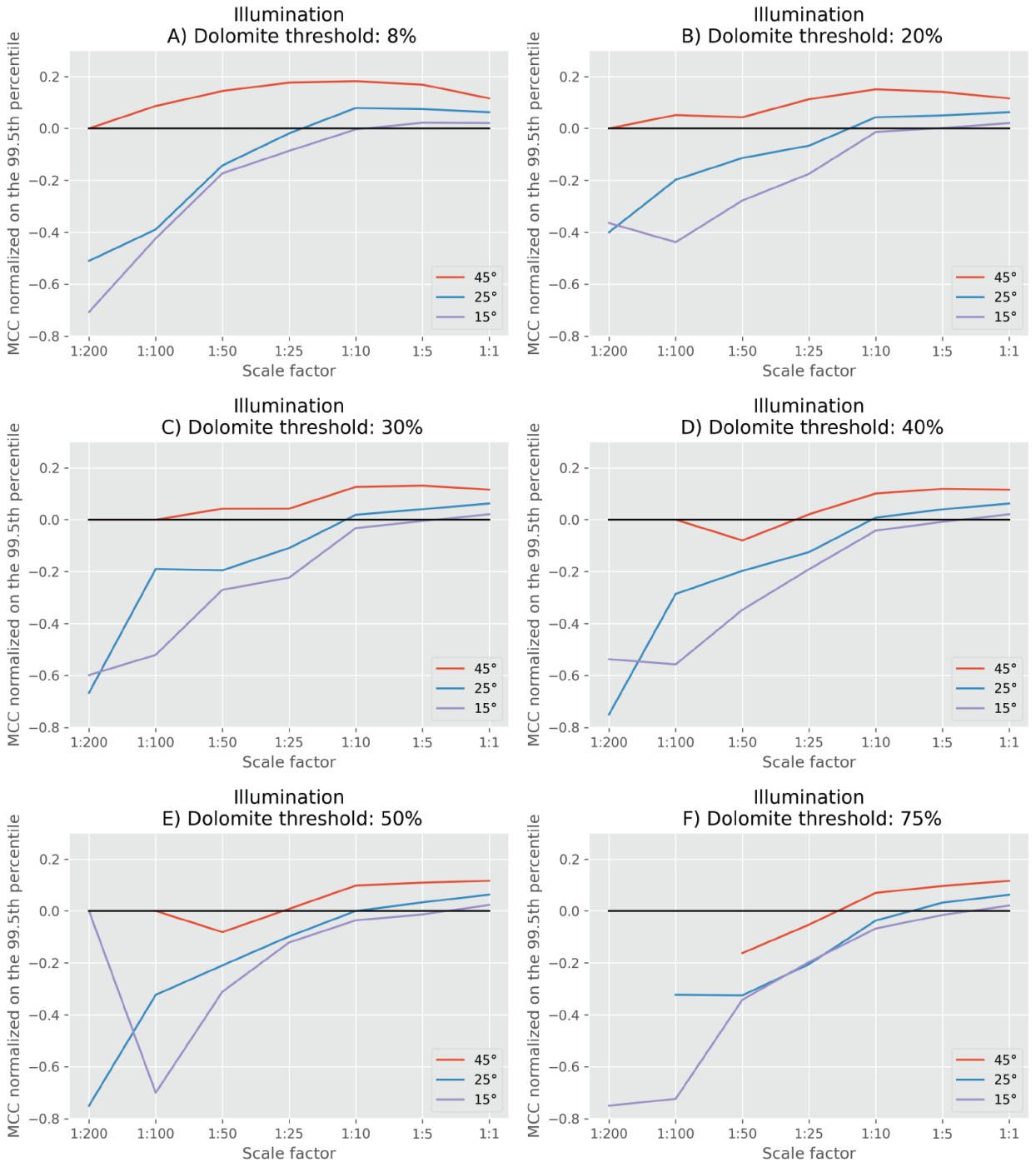

Figure 5.16: Trend in the significance of the illumination data. MCC has been normalized on the 99.5th percentile and then plotted. Everything over y = 0 is a significant result. Higher values represent a more correct prediction. Dolomite threshold: a) 8% Dolomite b) 20% dolomite c) 30% Dolomite d) 40% dolomite e) 50% dolomite f) 75% dolomite.

Case	Illumination angle	Directly significant	Inversely significant	Total	Success rate
1	45	26	0	33	79%
4	25	12	1	32	38%
5	15	10	2	30	33%

Table 5.8: The success rate of dolomite recognition by illumination angle

6 Discussion

6.1 Result summary

The most notable takeaways from the results are the observations:

- A change in frequency does not increase the success rate of the prediction of dolomite, but it does affect the quality of the successful predictions with a higher frequency producing higher quality predictions.
- A change in illumination and incident angle affects the success rate and quality of the successes. A lower illumination angle and a higher angle of incidence produce fewer successful predictions, and the successful predictions it does produce are of lower quality.
- Dolomites with more distinct elastic properties produce more successful predictions, and the predictions are of a higher quality. Due to an inverse significance, the dolomites with the lowest elastic properties can be predicted somewhat reliably in this geological setting.
- The downscaling reduces the number of significant predictions but does increase the quality of the predictions around the 10-fold downscaling. The best quality prediction scale varies with the dolomite threshold.
- Changing the dolomite threshold affects the number of significant predictions. An increased threshold reduces the number of successful predictions and reduces their quality.

6.2 Surfaces

The selected surface affects the ability to predict dolomite presences, with the Q4 surface performing slightly worse than the other surfaces and Q1 significantly worse. Since surfaces Q1, Q2 and Q3 are all completely within the Lower Thebes Formation; they are expected to have approximately the same chance for success. This expectation is supported by the observations in section 5.2 where no change in dolomite presence was observed with depth (with regards to the tilted orientation of the surfaces). A likely conclusion is that some surfaces are more challenging to predict caused by random factors such as their composition or the composition of the rock surrounding the surface. Surface Q0 is a special case as the layer underneath is completely homogenous in the model. It does have a higher-than-average success rate which can be attributed

to the underlying homogenous layer. Its success rate is not exceedingly high, and more research is required to confirm this trend.

6.3 Downscaling

Downscaling is the reduction of resolution used in this thesis to compare the dolomite occurrences by areas rather than individual data points (pixels).

The level of downscaling used affects the success rate in several ways. The success rate decreases as the RMS amplitude surface is downscaled more. A small amount of downscaling does not have a severe impact, but at the 1:25 scale, the effect becomes significantly greater. The effect of this quality decrease is amplified by increasing the dolomite threshold, such that for a dolomite threshold of 30% and higher, the usable scale decreases. This means that downscaling above 1:25 should not be used for dolomite prediction, a limit which should be reduced to 1:10 if a concentration of dolomite above 20% is the target.

The significance of the successful results peaks at a 1:10 scale, which means that the downscaled RMS surface is significantly more accurate in its predictions than an unscaled (1:1) RMS surface. This peak shifts as the dolomite threshold is increased. At a 30% threshold, it peaks at 1:5, and at a 40% threshold and above, it peaks at 1:1. This means that, when looking for smaller amounts of dolomite, it is better to use a downscaled RMS amplitude surface for dolomite prediction. When looking for high concentrations of dolomite, it is better to use an unscaled RMS amplitude surface to predict dolomite occurrences.

When predicting the presence of dolomite using a downscaled surface, the location becomes uncertain due to the gridding effect. It might be necessary to perform an evaluation to determine whether data with this level of uncertainty is helpful for research.

6.4 Frequency

A change in frequency does not affect how many successful predictions are made. It does increase the quality of the predictions that are already successful. The increase from 30Hz to 60Hz has the most significant effect, while a further increase to 90Hz does not increase the quality similarly. This means an increased frequency is desired as it gives a better image of the potential dolomite deposits. Frequency alone cannot create significant results if the other variables are poor. The benefit of an increase in frequency comes with diminishing returns, so investing in exceedingly high frequencies is probably unnecessary.

6.5 Illumination and incident angle

The illumination and incident angle significantly affect the ability to predict dolomite occurrences. The success rate is cut in half when the illumination angle is reduced from 45° to 25°. A further reduction to 15° does not have the same effect, but both 25° and 15° have low success rates. In addition, the quality of the predictions is reduced significantly as the illumination angle is reduced. The effect of these factors is so strong that an effort should be made to keep the illumination angle as high as possible.

It is possible that only one of the factors causes this significant drop in success rate. However, since the illumination and incident angles tend to change as a pair, it is unrealistic to vary these individually (Lecomte, 2008).

6.6 Elastic properties

The elastic properties significantly impact how well dolomite deposits can be predicted. As the density and velocity of the dolomite increase relative to the surrounding facies, the number of successful predictions increases significantly. This means that denser dolomite and dolomite with higher velocities are easier to predict. The density and compressional velocity of the dolomite might be affected by its contents (water or hydrocarbon) (Rogers, 2015), thus making dolomite with specific contents easier to locate. The effect of different contents, such as water and different hydrocarbons should be investigated further.

An interesting result is that the dolomite with the lowest possible values for velocity and density is similar to the matrix of the Lower Thebes Formation to the degree that it can be detected by the lack of RMS amplitude in that specific area. This presents an interesting dilemma as dolomite can be predicted with the presence and absence of an RMS amplitude peak depending on the type of dolomite and surrounding facies.

6.7 Success rates

The success rates referred to in this paper signify the number of predictions that pass the permutation test with p = 0.005. A success does not indicate that the prediction is 100% accurate, only that it is more accurate than 99.5% of the random attempts at predicting the dolomite deposits.

The Success rate never reaches 100% with the current setup, as the categories either contain all scale factors or all cases. The 1:200 and 1:100 scales rarely produce a successful prediction, and cases 6 and 9 rarely produce a positively successful prediction. Since 100% is unobtainable, the success rate might give a skewed indication of the performance. It might be better to perform the test on more horizons to increase the sample size instead of combining different scale factors and cases into one success rate.

6.8 Uncertainties

Throughout the modeling workflow, each aspect, from the data collection to the model generation to the statistical analysis, introduces a new source of uncertainty. Collecting the data in the field, data processing, data interpretation, and model creation all introduce a level of uncertainty.

Data collection in the field

Data collection cannot be done exhaustively and will therefore cause a certain level of uncertainty. Assumptions have to be made about the uniformity/continuity of formations. When analyzing the elastic properties, the location of the core plugs affects how a layer is represented, as it may not be uniform. The method used to determine the elastic properties also has potential sources of uncertainty. For this model, core plugs were used to measure these elastic properties. The samples used in core plug analysis are not large enough to analyze macro porosity. As there was macro

porosity (H. Corlett et al., 2021) in the outcrops used to construct the model, this has likely introduced uncertainty in the elastic properties gathered from the field.

Generating the model

A model based on outcrops comes with two caveats, outcrops are not always accessible for samples and close-up interpretation. A reasonable estimate can be made using high-resolution images and lidar data combined with property analyses from similar formations at other outcrops. The second caveat is that field data can only be collected in 1D or 2D, while the model is generated in 3D. This means that the shape, orientation, and frequency of the different geobodies have to be estimated to a certain degree. The behavior of the elastic properties throughout the model has been kept constant in this case, which works well as an estimation but may not be entirely accurate.

Since the model consists of homogenous cells, the geobody shape and internal variation of elastic properties are limited by the cell size. However, the latter is not an issue as facies are considered homogenous for this model.

Upscaling the model

The upscaling of a model reduces the size of the cells that make up the model. Upscaling a model will produce smoother seismic images with less aliasing (see figure 5.13) but will increase processing time. Upscaling also introduces a level of uncertainty into the workflow. Small degrees of upscaling produce only minor errors, but higher degrees of upscaling cause increasing degrees of errors (Milad et al., 2020).

Counteracting uncertainty

Uncertainty can be reduced generally at the cost of time. If more time is taken in the field to perform more samples, the uncertainty of the porosity values will be reduced. Creating a geocellular model with smaller cells will decrease the uncertainty, but the processing time will drastically increase. Increasing the sample size for the permutation test will reduce the uncertainty.

6.9 Issues

Issues with the surface selection

While creating the attribute surfaces for the model, a surface had to be chosen. The model included surfaces along which the cells were ordered. These cells, however, do not correspond to the actual boundaries of the different lithologies modeled and would not likely be a surface interpreted by geologists. The choice was made to use the provided horizons due to the difficulty of interpreting several horizons within the Lower Thebes Formation.

The complexity of the model

One of the significant challenges of this project is the fact that the model used is very complex. The subsurface's lithology frequently changes vertically and laterally, resulting in layers that are difficult to interpret on a seismic. Again the reason why model horizons have been chosen. The boundary between the upper and lower Thebes Formation is evident in the model as a packstone-dominated sequence is succeeded by a wackestone-dominated sequence. This boundary can also be observed on the seismic by the sudden change in amplitude. However, the boundary does not seem to coincide with either a trough or a peak, making it impossible to interpret this surface automatically.

The RMS amplitude cannot isolate individual dolomite deposits reliably, as there are several lithological transitions that cause seismic responses similar to dolomite (see table 4.4 in material and methods). The rapid vertical variation of facies may cause constructive or destructive interference, giving additional false positives and negatives for a dolomite occurrence.

Aliasing at higher frequencies

The synthetic seismic generated at 90Hz suffers from a problem similar to aliasing. The resolution of the seismic cube becomes too high cell size of the geocellular model, causing individual cells to be distinguishable on the seismic. The result is a seismic trace with a zig-zag pattern instead of smooth reflectors. This zig-zag pattern will also influence any horizon interpreted and affects 90Hz attributes projected onto a smooth horizon resulting in artifacts (see figure 4.8).

Unscaled RMS and model surfaces and the dolomite threshold

Since the script compares single pixels with a binary value, either hit or miss, the dolomite threshold does not impact the success rate of the unscaled predictions. The data point of unscaled pictures does, however, always line up with the trend of the data points that are affected by the dolomite threshold. This is not necessarily something that needs to be fixed, only something that should be noted.

6.10 Further research

Noise

All the results are currently generated without noise. In order to better represent real-life situations, noise should be added in varying degrees to analyze how different noise levels affect the performance of the dolomite prediction success rate.

Increasing the sample size

In order to get a large enough sample size to analyze the different cases, data has been combined from the different scale levels. In hindsight, this skews the data as the 1:200 scale RMS surfaces have a 0% success rate. By adding more horizons, the sample sizes can be filled with data generated with exactly the same parameters giving a more precise overview of the effect of each parameter.

Varying the surrounding facies

All facies have a range of possible elastic properties which will affect the seismic response, like the variation of elastic properties for dolomite did in this thesis. Further research could examine the possible ranges for the surrounding facies in this model and analyze their effect on the dolomite predictions.

Overburden and amplitude deprecation

In order to test the different frequencies properly, an overburden and amplitude deprecation function can be added. The method can then be performed with different overburdens to simulate the effect of depth on the success rate of dolomite detection.

Dolomite detection definition

For industry purposes, high quantities of reservoir rock are usually more interesting than smaller deposits. It might be possible to more reliably find more extensive deposits if "hits" are weighed based on how many adjacent "hits" it has. Large deposits will then become a more important factor in the success rate calculations, while smaller deposits will have less effect giving a more interesting prediction for industry purposes.

Wavelet

Although changing the wavelet in addition to the other attributes may result in interesting findings, it is beyond the scope of this thesis. It could be the subject of further research.

Script

The script can be improved in several ways. One is to allow for grayscale images of the RMS surface, which allows for faster tweaking of the threshold values instead of changing the threshold in Petrel and then exporting the images again. In this case, individual thresholds should be assigned per image or estimated in some way. Another improvement would be to implement a proprietary file system that would represent the images instead of using actual images for the processing, this would drastically speed up the process, and the proprietary file could be transformed into an image at a later point if necessary.

7 Conclusion

The aim of this thesis was to improve the understanding of how dolomites are imaged and can be interpreted from seismic data. A part of this aim was determining the effect of several parameters on the seismic and the ability to predict dolomite deposits from it. From the results discussed above, the following main conclusions can be made:

- Dolomite geobody locations can be predicted with a significant degree of success using RMS amplitude, and the success rate depends on some of the parameter values.
- Illumination and incident angles significantly impact the ability to predict dolomite geobodies; higher illumination angles and lower incident angles yield better results.
- The dominant frequency does not affect the success rate of the predictions, and it will not turn an unsuccessful prediction into a success. However, it will enhance the quality of successful predictions.
- Using a downscaled version of the RMS amplitude surface enhances the performance of predictions made for some scales. The best scale is dependent on the dolomite threshold level. The thesis has not generated enough data to determine the exact relationship between the best scale and the dolomite threshold.
- Elastic properties affect the detection rate of the dolomite, with higher values giving a better chance for a significant result.
- Dolomite with low elastic property values can be detected with a significant success rate, using the troughs of the RMS attribute surface instead of the peaks. This may only be possible because the elastic properties are similar to the dominating facies'
- An unidentified factor affects the success rate of a dolomite prediction based on the surface used for the interpretation. As all obvious parameters are accounted for, it is likely due to random chance based on the composition of the surface and surrounding volume.

8 References

Allan, J. R., & Wiggins, W. D. (1993). *Dolomite reservoirs: Geochemical techniques for evaluating origin and distribution*. American Association of Petroleum Geologists.

Bosworth, W. (2015). Geological Evolution of the Red Sea: Historical Background, Review, and Synthesis. In N. M. A. Rasul & I. C. F. Stewart (Eds.), *The Red Sea* (pp. 45–78). Springer Berlin Heidelberg. https://doi.org/10.1007/978-3-662-45201-1_3

Bosworth, W., Guiraud, R., & Kessler, L. G. (1999). Late Cretaceous (ca. 84 Ma) compressive deformation of the stable platform of northeast Africa (Egypt): Far-field stress effects of the "Santonian event" and origin of the Syrian arc deformation belt. *Geology*, *27*(7), 633. https://doi.org/10.1130/0091-7613(1999)027<0633:LCCMCD>2.3.CO;2

Chen, G., Cox, R. W., Glen, D. R., Rajendra, J. K., Reynolds, R. C., & Taylor, P. A. (2019). A tail of two sides: Artificially doubled false positive rates in neuroimaging due to the sidedness choice with *t* -tests. *Human Brain Mapping*, *40*(3), 1037–1043. https://doi.org/10.1002/hbm.24399

Chicco, D., & Jurman, G. (2020). The advantages of the Matthews correlation coefficient (MCC) over F1 score and accuracy in binary classification evaluation. *BMC Genomics*, *21*(1), 6. https://doi.org/10.1186/s12864-019-6413-7

Corlett, H., Hodgetts, D., Hirani, J., Rotevatn, A., Taylor, R., & Hollis, C. (2021). A geocellular modelling workflow for partially dolomitized remobilized carbonates: An example from the Hammam Faraun Fault block, Gulf of Suez, Egypt. *Marine and Petroleum Geology*, *126*, 104831. https://doi.org/10.1016/j.marpetgeo.2020.104831

Corlett, H. J., Bastesen, E., Gawthorpe, R. L., Hirani, J., Hodgetts, D., Hollis, C., & Rotevatn, A. (2018). Origin, dimensions, and distribution of remobilized carbonate deposits in a tectonically

active zone, Eocene Thebes Formation, Sinai, Egypt. *Sedimentary Geology*, *372*, 44–63. https://doi.org/10.1016/j.sedgeo.2018.04.008

Davies, M. R. (2018). Emerging Technologies: Machine Learning. *CSEG Recorder | January 2018*, *43*(1), 48.

Demir, F. (2022). Deep autoencoder-based automated brain tumor detection from MRI data. In *Artificial Intelligence-Based Brain-Computer Interface* (pp. 317–351). Elsevier. https://doi.org/10.1016/B978-0-323-91197-9.00013-8

Egypt Concession Map. (2022). [Map]. Egypt upstream gateway. https://eug.petroleum.gov.eg/dp/pages/customcode/MDS_iTabs/information-img/Egypt_Concession_Map.pdf

Ehrhardt, A., & Hübscher, C. (2015). The Northern Red Sea in Transition from Rifting to Drifting-Lessons Learned from Ocean Deeps. In N. M. A. Rasul & I. C. F. Stewart (Eds.), *The Red Sea* (pp. 99–121). Springer Berlin Heidelberg. https://doi.org/10.1007/978-3-662-45201-1_5

El-Motaal, E. A., & Kusky, T. M. (2003). *TECTONIC EVOLUTION OF THE INTRAPLATE S-SHAPED SYRIAN ARC FOLD-THRUST BELT OF THE MIDDLE EAST REGION IN THE CONTEXT OF PLATE TECTONICS*. 20.

Fahimuddin, A., Aanonsen, S. I., & Skjervheim, J.-A. (2010). *4D Seismic History Matching of a Real Field Case with EnKF: Use of Local Analysis for Model Updating*. SPE-134894-MS. https://doi.org/10.2118/134894-MS

Gawthorpe, R. L., Jackson, C. A.-L., Young, M. J., Sharp, I. R., Moustafa, A. R., & Leppard, C. W. (2003). Normal fault growth, displacement localisation and the evolution of normal fault populations: The Hammam Faraun fault block, Suez rift, Egypt. *Journal of Structural Geology*, *25*(6), 883–895. https://doi.org/10.1016/S0191-8141(02)00088-3

Geldart, L. P., & Sheriff, R. E. (2004). *Problems in Exploration Seismology and their Solutions*. Society of Exploration Geophysicists. https://doi.org/10.1190/1.9781560801733

Gholamy, A., & Kreinovich, V. (2014). Why Ricker wavelets are successful in processing seismic data: Towards a theoretical explanation. *2014 IEEE Symposium on Computational Intelligence for Engineering Solutions (CIES)*, 11–16. https://doi.org/10.1109/CIES.2014.7011824

Hamimi, Z., El-Barkooky, A., Martínez Frías, J., Fritz, H., & Abd El-Rahman, Y. (Eds.). (2020). *The Geology of Egypt*. Springer International Publishing. https://doi.org/10.1007/978-3-030-15265-9

He, T., & Schmitt, D. R. (2006). Velocity measurements of conglomerates and pressure sensitivity analysis of AVA response. *SEG Technical Program Expanded Abstracts 2006*, 1888–1892. https://doi.org/10.1190/1.2369894

Hollis, C., Corlett, H., Hirani, J., Hodgetts, D., Gawthorpe, R., Rotevatn, A., & Bastesen, E. (2013). *Quantification of Depositional and Diagenetic Geobody Geometries for Reservoir Modelling, Hammam Fauran Fault Block, Sinai Peninsula, Egypt*. 75th EAGE Conference and Exhibition - Workshops, London, UK. https://doi.org/10.3997/2214-4609.20131226

Höntzsch, S., Scheibner, C., Guasti, E., Kuss, J., Marzouk, A. M., & Rasser, M. W. (2011). Increasing restriction of the Egyptian shelf during the Early Eocene? — New insights from a southern Tethyan carbonate platform. *Palaeogeography, Palaeoclimatology, Palaeoecology*, *302*(3–4), 349–366. https://doi.org/10.1016/j.palaeo.2011.01.022

Jackson, C. A. L., Gawthorpe, R. L., Leppard, C. W., & Sharp, I. R. (2006). Rift-initiation development of normal fault blocks: Insights from the Hammam Faraun fault block, Suez Rift, Egypt. *Journal of the Geological Society*, *163*(1), 165–183. https://doi.org/10.1144/0016-764904-164

Jones, I. F., & Davison, I. (2014). Seismic imaging in and around salt bodies. *Interpretation*, *2*(4), SL1–SL20. https://doi.org/10.1190/INT-2014-0033.1

Kallweit, R. S., & Wood, L. C. (1982). The limits of resolution of zero-phase wavelets. *GEOPHYSICS*, *47*(7), 1035–1046. https://doi.org/10.1190/1.1441367

Lecomte, I. (2008). Resolution and illumination analyses in PSDM: A ray-based approach. *The Leading Edge*, *27*(5), 650–663. https://doi.org/10.1190/1.2919584

Lecomte, I., & Kaschwich, T. (2008). *Closer to Real Earth In Reservoir Characterization: A 3D Isotropic/anisotropic PSDM Simulator.* SEG-2008-1570.

Lecomte, I., Lavadera, P. L., Anell, I., Buckley, S. J., Schmid, D. W., & Heeremans, M. (2015). Ray-based seismic modeling of geologic models: Understanding and analyzing seismic images efficiently. *Interpretation*, *3*(4), SAC71–SAC89. https://doi.org/10.1190/INT-2015-0061.1

Lecomte, I., Lubrano-Lavadera, P., Botter, C., Anell, I., Buckley, S., Eide, C., Grippa, A., Mascolo, V., & Kjoberg, S. (2016). 2(3)D convolution modelling of complex geological targets—Beyond 1D convolution. *First Break*, *34*, 99–107. https://doi.org/10.3997/1365-2397.34.5.84451

Milad, B., Ghosh, S., Slatt, R., Marfurt, K., & Fahes, M. (2020). Practical Aspects of Upscaling Geocellular Geological Models for Reservoir Fluid Flow Simulations: A Case Study in Integrating Geology, Geophysics, and Petroleum Engineering Multiscale Data from the Hunton Group. *Energies*, *13*(7), 1604. https://doi.org/10.3390/en13071604

Morton-Thompson, D., Woods, A. M., & American Association of Petroleum Geologists (Eds.). (1993). *Development geology reference manual*. American Association of Petroleum Geologists.

Moustafa, A. R. (2014). Structural architecture and tectonic evolution of the Maghara inverted basin, Northern Sinai, Egypt. *Journal of Structural Geology*, *62*, 80–96. https://doi.org/10.1016/j.jsg.2014.01.014

Moustafa, A. R., & Abdeen, M. M. (1992). Structural setting of the Hammam Faraun block, eastern side of the Suez rift. *Journal of the University of Kuwait*, *19*(2), 291–310.

Moustafa, A. R., & Khalil, M. H. (1995). SUPERPOSED DEFORMATION IN THE NORTHERN SUEZ RIFT, EGYPT: RELEVANCE TO HYDROCARBONS EXPLORATION. *Journal of Petroleum Geology*, *18*(3), 245–266. https://doi.org/10.1111/j.1747-5457.1995.tb00905.x

Moustafa, A. R., & Khalil, S. M. (2017). Control of extensional transfer zones on syntectonic and post-tectonic sedimentation: Implications for hydrocarbon exploration. *Journal of the Geological Society*, *174*(2), 318–335. https://doi.org/10.1144/jgs2015-138

Oldenburg, D., Jones, F., Heagy, L., Astic, T., Cockett, R., Devriese, S., Kang, S., & Capriotti, J. (2017). *Geophysics for Practicing Geoscientists—GPG 0.0.1 documentation*. https://gpg.geosci.xyz/index.html

Raji, W., & Rietbrock, A. (2013). Attenuation (1/ *Q*) estimation in reflection seismic records. *Journal of Geophysics and Engineering*, *10*(4). https://doi.org/10.1088/1742-2132/10/4/045012

Rogers, R. (2015). Deep Ocean Sediment–Hydrate Relationships. In *Offshore Gas Hydrates* (pp. 21–63). Elsevier. https://doi.org/10.1016/B978-0-12-802319-8.00002-4

Scheibner, C., Kuss, J., & Speijer, R. P. (2003). Stratigraphic modelling of carbonate platform-to-basin sediments (Maastrichtian to Paleocene) in the Eastern Desert, Egypt. *Palaeogeography, Palaeoclimatology, Palaeoecology*, *200*(1–4), 163–185. https://doi.org/10.1016/S0031-0182(03)00449-8

Scheibner, C., Marzouk, A. M., & Kuss, J. (2001). Shelf architectures of an isolated Late Cretaceous carbonate platform margin, Galala Mountains (Eastern Desert, Egypt). *Sedimentary Geology*, *145*(1–2), 23–43. https://doi.org/10.1016/S0037-0738(01)00114-2

Schön, J. (2011). *Physical properties of rocks: A workbook*. Elsevier.

Schön, J. (2015). *Physical properties of rocks: Fundamentals and principles of petrophysics* (2nd edition). Elsevier.

Simm, R., & Bacon, M. (2014). *Seismic Amplitude: An Interpreter's Handbook*. Cambridge University Press. https://doi.org/10.1017/CBO9780511984501

Sukmono, S. (2010, January 5). Fundamental Issues on the Application of seismic Methodologies for Carbonate Reservoir Characterization. *Proc. Indon Petrol. Assoc., 34th Ann. Conv.* Thirty-Fourth Annual Convention. https://doi.org/10.29118/IPA.2570.10.G.108

Urone, P. P., & Hinrichs, R. (2018). *Douglas College Physics 1207*. Pressbooks.

Wood, D. A., & Cai, J. (Eds.). (2022). *Sustainable geoscience for natural gas subsurface systems*. Gulf Professional Publishing, an imprint of Elsevier.

Young, M. J., Gawthorpe, Rob. L., & Sharp, I. R. (2003). Normal fault growth and early syn-rift sedimentology and sequence stratigraphy: Thal Fault, Suez Rift, Egypt: Thal Fault, Suez Rift, Egypt. *Basin Research*, *15*(4), 479–502. https://doi.org/10.1046/j.1365-2117.2003.00216.x

Youssef, M. M. (2003). Structural setting of central and south Egypt: An overview. *Micropaleontology*, *49*(Suppl_1), 1–13. https://doi.org/10.2113/49.Suppl_1.1

9 Appendix

Appendix 1: Step-by-step walkthrough of the process for synthetic seismic

Attached separately.

Appendix 2: Python code for generating downscaled images

Attached separately.

Appendix 3: Python code for analyzing performance metric of downscaled images

Attached separately.

Appendix 4: Code for plotting normalized MCC data

Attached separately.